A 3-D numerical model of the influence of meanders on groundwater discharge to a gaining stream in an unconfined sandy aquifer

Balbarini, Nicola; Boon, Wietse M.; Nicolajsen, Ellen ; Nordbotten, Jan M.; Bjerg, Poul Løgstrup; Binning, Philip John

Published in:
Journal of Hydrology

Link to article, DOI:
10.1016/j.jhydrol.2017.06.042

Publication date:
2017

Document Version
Peer reviewed version

A 3-D numerical model of the influence of meanders on groundwater discharge to a gaining stream in an unconfined sandy aquifer

Nicola Balbarini[1], Wietse M. Boon[2], Ellen Nicolajsen[1], Jan M. Nordbotten[2,3], Poul L. Bjerg[1] and Philip J. Binning[1]

[1]Department of Environmental Engineering, Technical University of Denmark, Kgs. Lyngby, Denmark, [2] Department of Mathematics, University of Bergen, Bergen, Norway, [3] Department of Civil and Environmental Engineering, Princeton University, Princeton, New Jersey, USA

Corresponding author: Nicola Balbarini, Department of Environmental Engineering, Technical University of Denmark, Bygningstorvet, Building 115, DK – 2800 Kgs. Lyngby, Denmark, (nbal@env.dtu.dk)

Journal: Journal of Hydrology

Revised submission March 2017

Minor revisions May 2017

Key words: Numerical model, 3-D, Meander, Stream geometry, Spatial and temporal variability, Reach scale.

Abstract

Groundwater discharge to streams depends on stream morphology and groundwater flow direction, but are not always well understood. Here a 3-D groundwater flow model is employed to investigate the impact of meandering stream geometries on groundwater discharge to streams in an unconfined and homogenous sandy aquifer at the reach scale (10-200 m). The effect of meander geometry was examined by considering three scenarios with varying stream sinuosity. The interaction with regional groundwater flow was examined for each scenario by considering three groundwater flow directions. The sensitivity of stream morphology and flow direction to other parameters was quantified by varying the stream width, the meander amplitude, the magnitude of the hydraulic gradient, the hydraulic conductivity, and the aquifer thickness. Implications for a real stream were then investigated by simulating groundwater flow to a stream at a field site located in Grindsted, Denmark. The simulation of multiple scenarios was made possible by the employment of a computationally efficient coordinate transform numerical method. Comparison of the scenarios showed that the geometry of meanders greatly affect the spatial distribution of groundwater flow to streams. The shallow part of the aquifer discharges to the outward pointing meanders, while deeper groundwater flows beneath the stream and enters from the opposite side. The balance between these two types of flow depends on the aquifer thickness and meander geometry. Regional groundwater flow can combine with the effect of stream meanders and can either enhance or smooth the effect of a meander bend, depending on the regional flow direction. Results from the Grindsted site model showed that real meander geometries had similar effects to those observed for the simpler sinuous streams, and showed that despite large temporal variations in stream discharge, the spatial pattern of flow is almost constant in time for a gaining stream.

1. Introduction

An understanding of the interaction between groundwater and streams is needed to map water fluxes and the transport of contaminants from groundwater into streams (Cey et al., 1998; Derx et al., 2010; Anibas et al., 2012; Karan et al., 2013; Ou et al., 2013; Freitas et al., 2015). This interaction is governed by several factors such as the hydraulic gradient between the aquifer and the stream, the stream channel geometry, and the hydraulic conductivity distribution of the aquifer and the streambed (Larkin and Sharp, 1992; Cey et al., 1998; Krause et al., 2007; Anibas et al., 2012; Binley et al., 2013; Fernando, 2013; Flipo et al., 2014). Furthermore, flow processes between groundwater and streams are scale dependent and so must be investigated at different scales (Dahl et al., 2007; Anibas et al., 2012; Flipo et al., 2014; Poulsen et al., 2015).

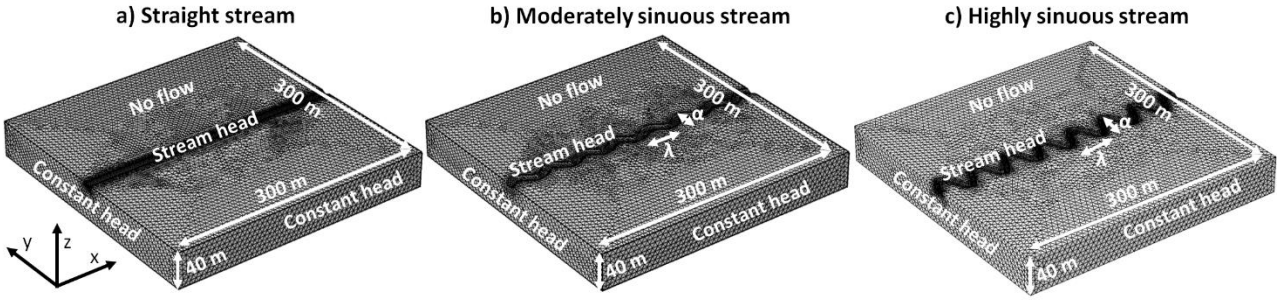

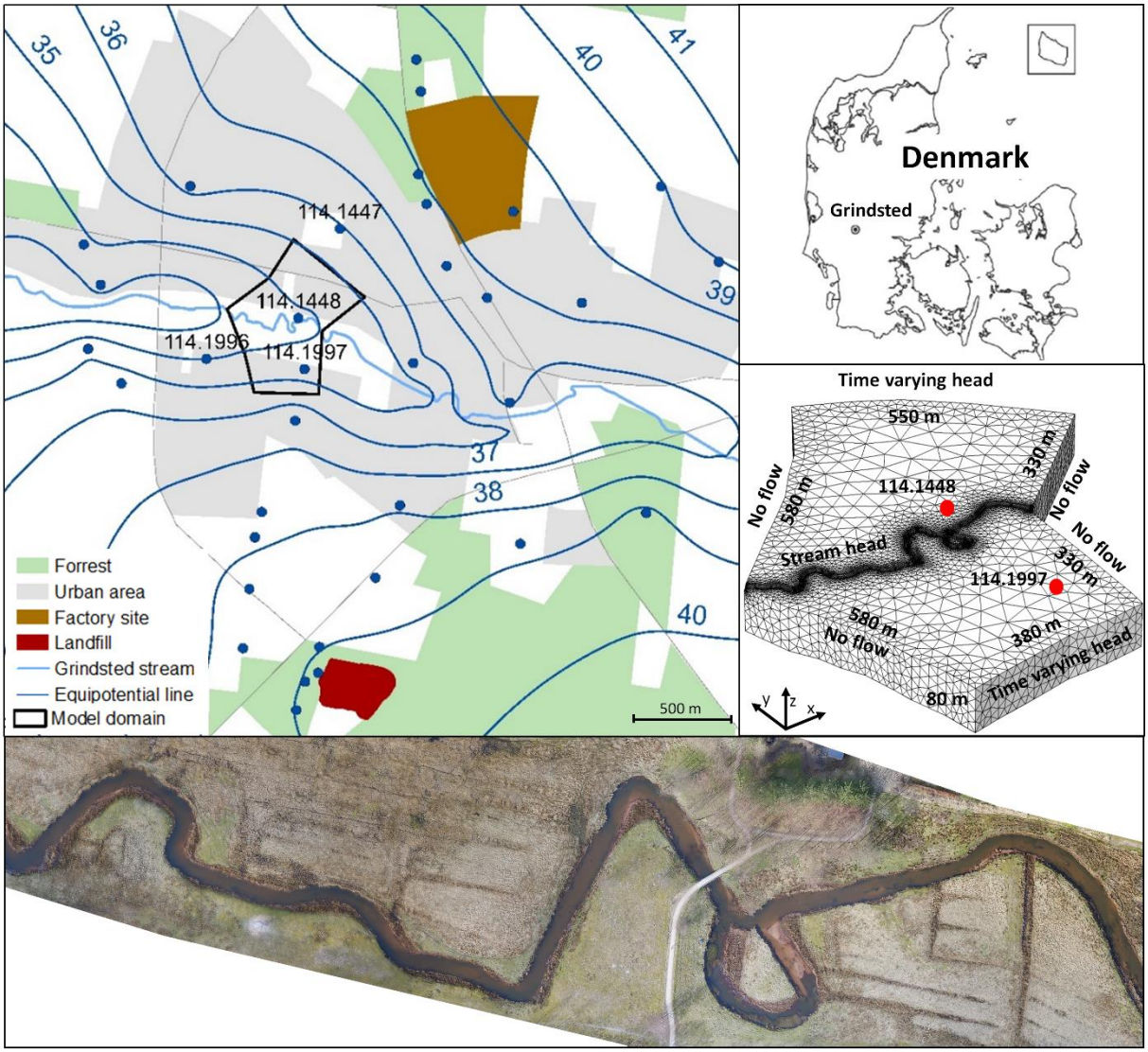
35
36
40
41
39
37
38
40
114.1447
114.1448
114.1996
114.1997
Forrest
Urban area
Factory site
Landfill
Grindsted stream
Equipotential line
Model domain
500 m
Denmark
Grindsted
Time varying head
550 m
330 m
No flow
580 m
114.1448
No flow
Stream head
No flow
330 m
114.1997
580 m
No flow
380 m
Time varying head
80 m
y
z
x

57

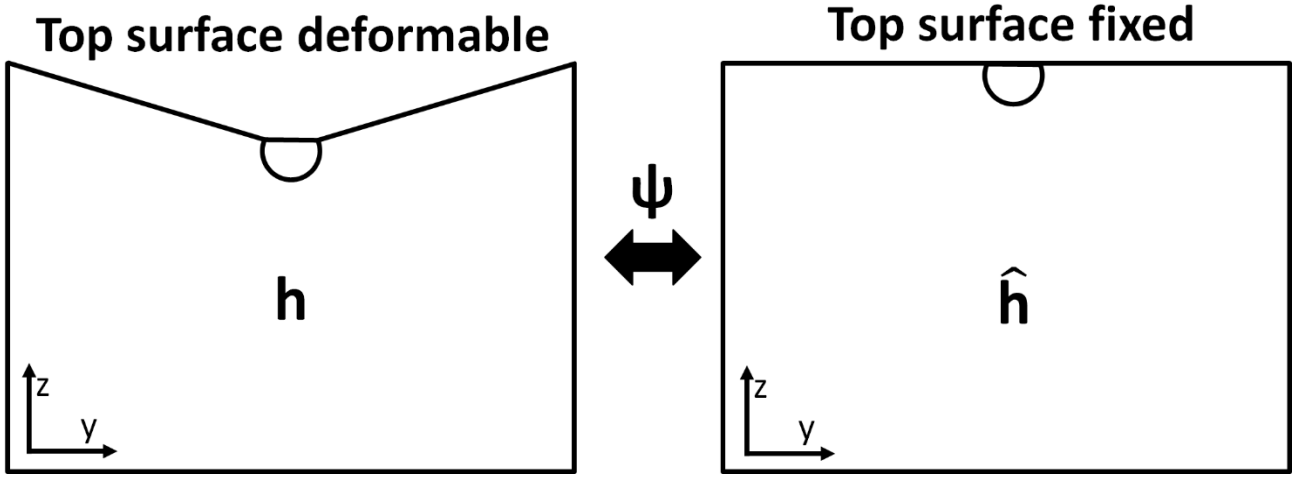
Top surface deformable
h
z
y
ψ
Top surface fixed
ĥ
z
y

58

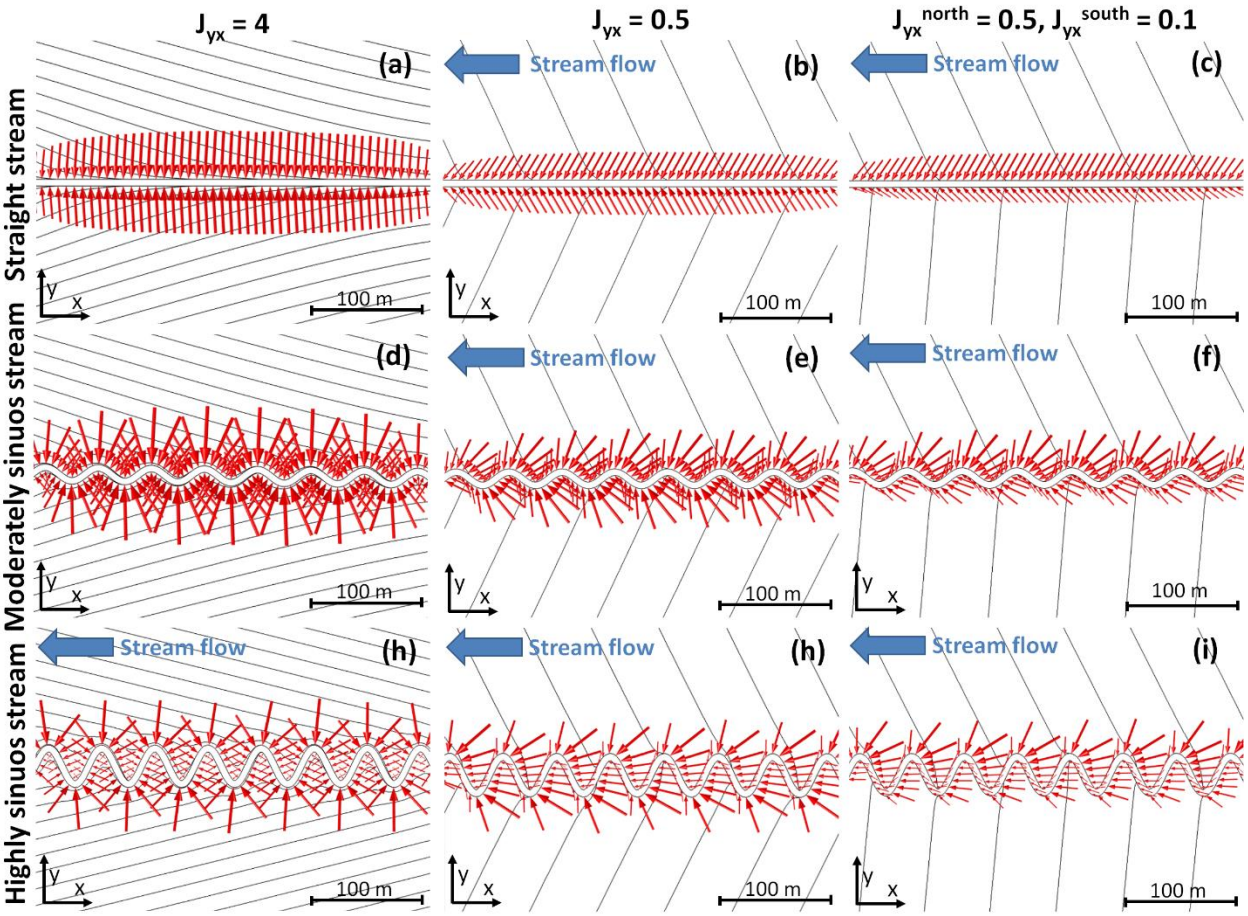
J_{yx} = 4
J_{yx} = 0.5
J_{yx}^{north} = 0.5, J_{yx}^{south} = 0.1
Straight stream
Moderately sinuos stream
Highly sinuos stream
Stream flow
(a)
(b)
(c)
(d)
(e)
(f)
(h)
(h)
(i)
100 m
y
x

59

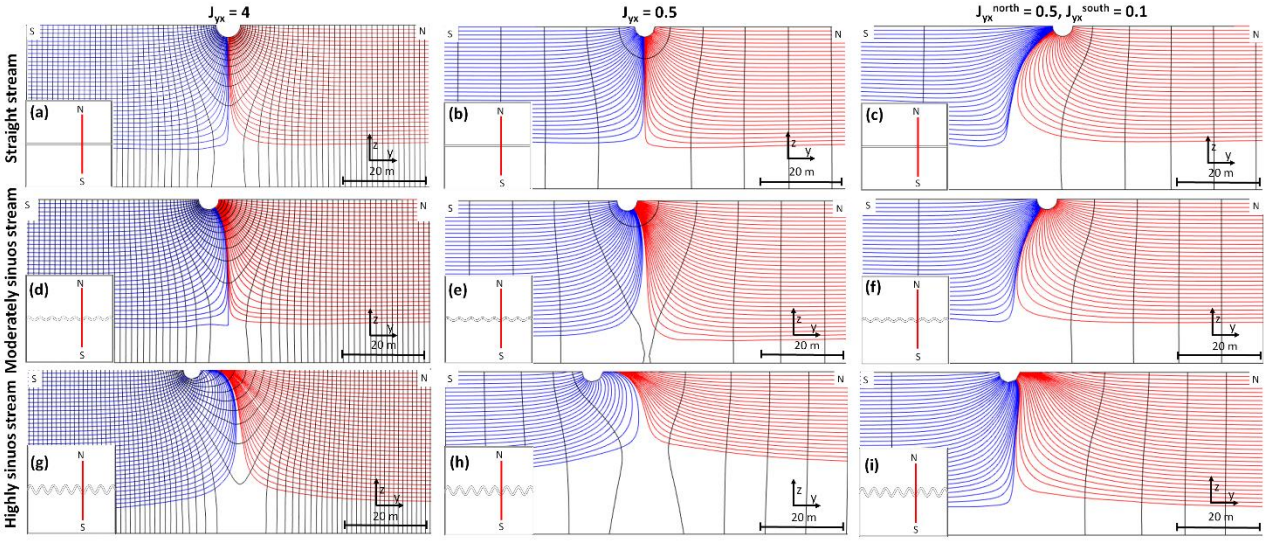
J_{yx} = 4
J_{yx} = 0.5
J_{yx}^{north} = 0.5, J_{yx}^{south} = 0.1
Straight stream
Moderately sinuos stream
Highly sinuos stream
(a)
(b)
(c)
(d)
(e)
(f)
(g)
(h)
(i)
N
S
20 m

60

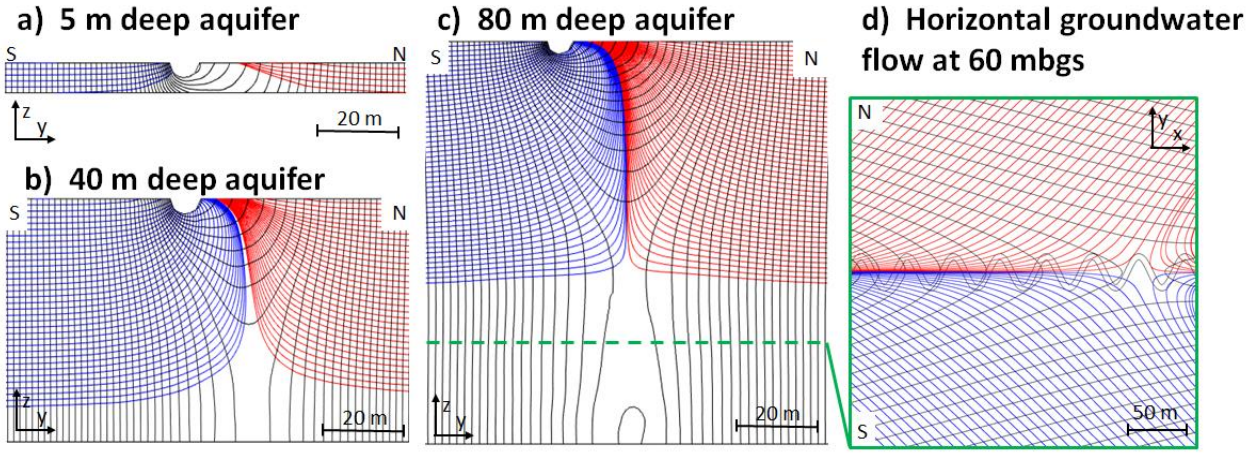
a) 5 m deep aquifer
S
N
z
y
20 m
b) 40 m deep aquifer
S
N
z
y
20 m
c) 80 m deep aquifer
S
N
z
y
20 m
d) Horizontal groundwater flow at 60 mbgs
N
y
x
S
50 m

61

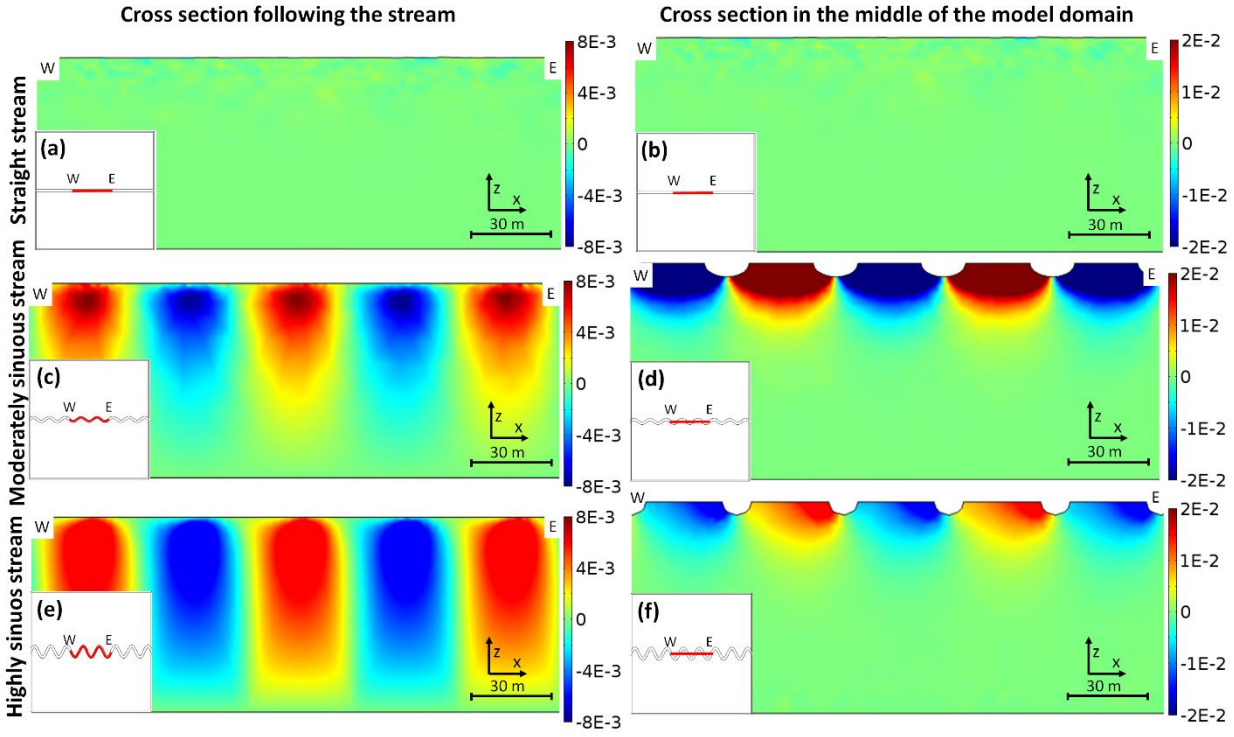
Cross section following the stream
Cross section in the middle of the model domain
Straight stream
Moderately sinuous stream
Highly sinuos stream
W
E
(a)
(b)
(c)
(d)
(e)
(f)
30 m
8E-3
4E-3
0
-4E-3
-8E-3
2E-2
1E-2
0
-1E-2
-2E-2

62

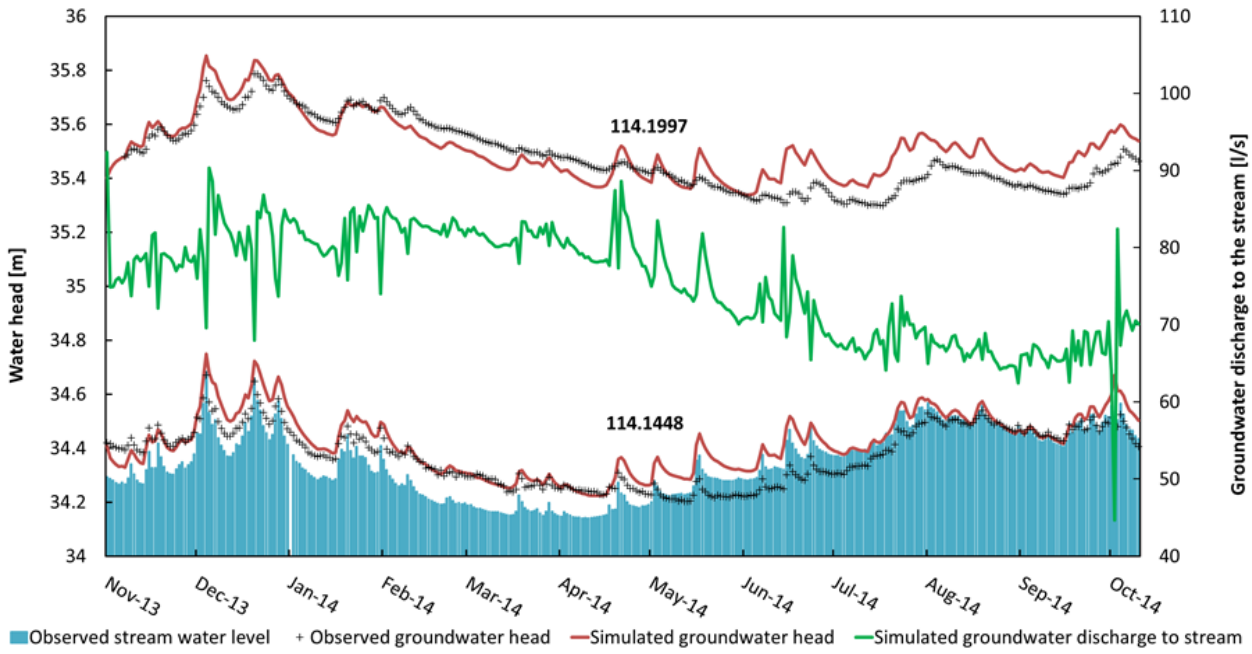
Water head [m]
Groundwater discharge to the stream [l/s]
114.1997
114.1448
Nov-13
Dec-13
Jan-14
Feb-14
Mar-14
Apr-14
May-14
Jun-14
Jul-14
Aug-14
Sep-14
Oct-14
Observed stream water level
Observed groundwater head
Simulated groundwater head
Simulated groundwater discharge to stream

63

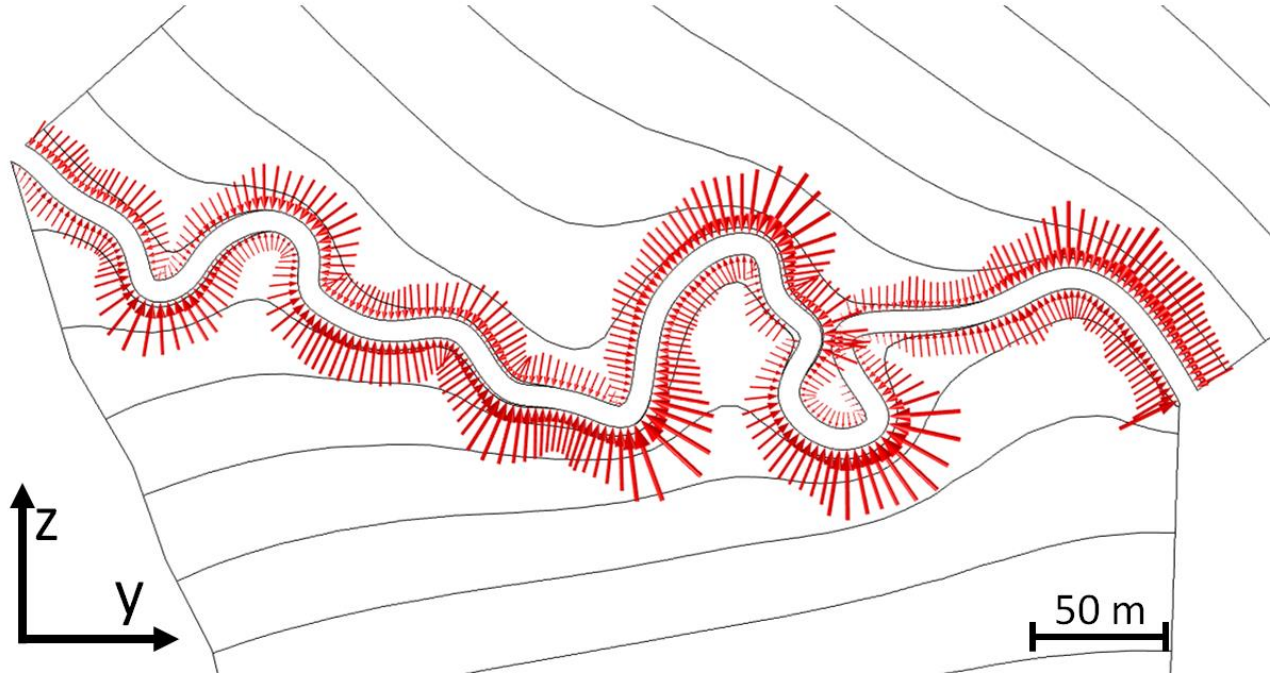
z
y
50 m

64

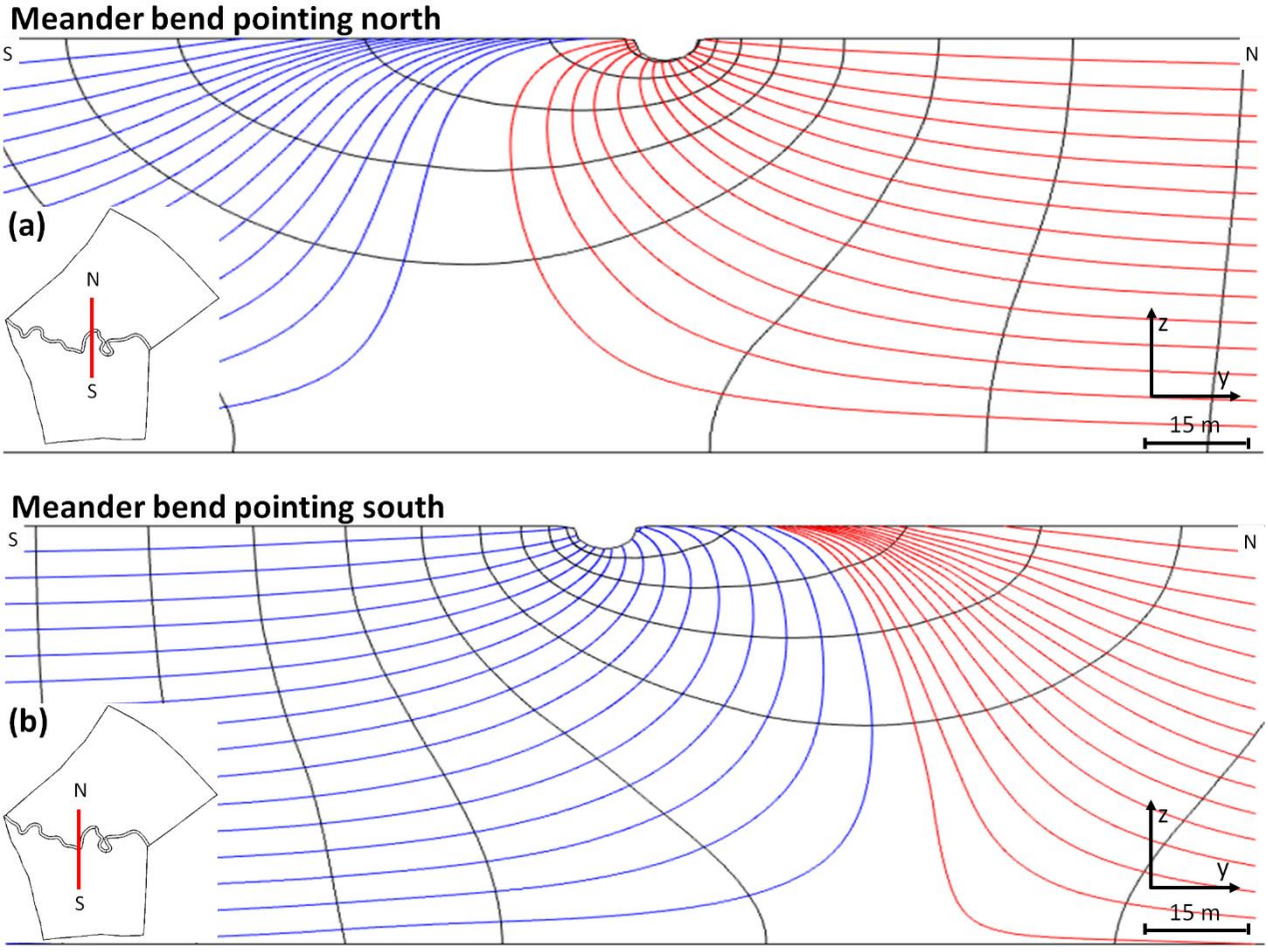

At the reach scale (10-200 m), groundwater flow to streams is both vertical and horizontal; thus, an analysis in three-dimensions is required (Harvey and Bencala, 1993; Modica et al., 1998; Flipo et al., 2014). Reach scale groundwater flow paths to streams are not adequately resolved at the larger regional or catchment scales considered by Toth (1963) and many other later larger scale studies (e.g. Larkin and Sharp, 1992; Wroblicky et al., 1998; Modica et al., 1998; Anibas et al., 2012; Aisopou et al., 2015a; Flipo et al., 2014; Gomez-Velez et al., 2015).

Studies investigating reach scale groundwater flow to streams have generally considered straight streams, and have not accounted for the effect of meander bends (Derx et al., 2010; Guay et al., 2013; Miracapillo and Morel-Seytoux, 2014, see also overview in Table S1). Thus, a better understanding of how groundwater flow varies in space because of stream meanders is needed (Modica et al., 1998; Diem et al., 2014; Krause et al., 2014; Boano et al., 2014). This is particularly

77 important when investigating contaminant plume discharge to a stream system, where insight is
78 needed to improve site investigations, data interpretation and to design more efficient monitoring
79 campaigns (Harvey and Bencala, 1993; Conant et al., 2004; Anibas et al., 2012; Weatherill et al.,
80 2014). The appropriate scale for contaminant plume studies will often be similar to the stream reach
81 scale (Conant et al., 2004; Byrne et al., 2014; Weatherill et al., 2014; Freitas et al., 2015).
82 Only a few studies have analyzed groundwater flow to meandering streams (e.g. Dahl et al.
83 (2007), Nalbantis et al. (2011), Flipo et al. (2014), and Boano et al. (2014)). A literature review is
84 shown in Table S1 and shows that the majority of research on meandering stream-aquifer interaction
85 has focused on the hyporheic exchange processes (Wroblicky et al., 1998; Salehin et al., 2004;
86 Cardenas et al., 2004; Cardenas 2008; Revelli et al., 2008; Cardenas, 2009a; Cardenas, 2009b; Boano
87 et al., 2006; Stonedahl et al., 2010; Boano et al., 2009; Boano et al., 2010, Brookfield and Sudicky,
88 2013; Gomez-Velez et al., 2014; Gomez-Velez et al., 2015). Hyporheic exchange processes take
89 place in the hyporheic zone just under the stream bed, where stream water mixes with groundwater,
90 before returning to the stream. For example, Boano et al. (2010) applied an analytical approach to
91 examine 3-D groundwater flows directly under a streambed, but did not consider the surrounding
92 groundwater flow system.
93 For many problems, it is necessary to move beyond the hyporheic zone, and consider larger
94 scale groundwater flows at the reach scale. Thus, the focus of this paper is groundwater flow to
95 meandering streams at the reach scale.
96 This study analyses the spatial variability of the groundwater flow discharge to streams along
97 meander bends in a full 3-D system at the reach scale. The first aim is to simulate the groundwater
98 flow paths to streams and investigate how those paths are affected by stream meanders and
99 groundwater flow direction in an unconfined sandy aquifer. A 3-D numerical model is presented
100 simulating the discharge to streams for a synthetic gaining sinuous stream with three scenarios of

sinuosity: a straight stream, a moderately sinuous stream, and a highly sinuous stream. For each scenario, three groundwater flow directions are assumed with the dominant groundwater flow being: perpendicular to the stream; along the stream; and diagonally across the stream. The resulting groundwater flow to the stream for different sinuosities was quantified for different stream widths, meander geometries, aquifer thicknesses, homogenous hydraulic conductivities, and hydraulic gradients in order to assess the combined effects and the robustness of the results. All numerical models were designed to simulate the groundwater flow to the stream, disregarding the hyporheic flow. The second aim is to apply the 3-D numerical model to a meandering stream at Grindsted in Denmark in order to assess the effects in a field scale system (unconfined, sandy aquifer) with a real geometry and time varying stream water levels. Finally, the implications for our current understanding of discharges to streams are discussed.

To address these aims, the 3-D numerical model employed a novel coordinate transformation method developed by Boon et al. (2016). This method solves the equation for groundwater flow in a transformed domain, which is constant in time, while the coordinate system changes depending on the groundwater free surface variations. The application of the linear transformation allows the transformed domain geometry to be simpler than the original problem; thus, the method is computationally efficient and can be applied to complex geometries. Boon et al. (2016) employs the method to simulate groundwater flow to wells, but it has not been applied to other relevant groundwater systems. Since the application of the coordinate transform method to groundwater/surface water interaction is new, it was first tested and compared to existing approaches (the moving mesh and the saturated-unsaturated groundwater flow method). It is shown that the coordinate transform method is far more computationally efficient than the other methods (see Supporting Information, Section S1).

2. Method

2.1 Sinusoidal stream model

In this study, the effect of the stream sinuosity on the groundwater flow to streams is analyzed by extending the two-dimensional steady state model developed by Cardenas (2009a; 2009b) to three dimensions. The stream is assumed to be sinusoidal with a constant wavelength (λ) of 40 m and amplitude (α), which is varied in order to reproduce different levels of sinuosity. The sinuosity (S) is calculated by dividing the sinuous stream length along the channel by the straight valley length (300 m in this study). Three sinuosity scenarios (Figure 1) are considered: a) straight stream (S=1, α=0 m), b) moderately sinuous stream (S=1.14, α=5 m), and c) a highly sinuous stream (S=1.74, α=13.5 m). The choices of sinuosity, wavelength, and amplitude are the same as those of Cardenas (2009a; 2009b).

The spatial variability of the groundwater flow to the stream is affected by the stream morphology, the groundwater flow direction, and the distribution of hydraulic conductivities (Krause et al, 2012; Gomez-Velez et al., 2014). In order to isolate and analyze the effect of the stream morphology and the groundwater flow direction, the aquifer is assumed to be homogenous and isotropic with a hydraulic conductivity of 40 m/d. The stream cross section is a half-ellipsoidal with a depth of 3 m and a width of 5 m. The stream-aquifer interface is a constant-head boundary where the head varies linearly along the channel with a gradient determined by dividing the overall gradient in the x-direction (0.001) by the sinuosity. Thus, the stream is a gaining stream along the entire length. The top and bottom boundary, except for the stream boundary, are no-flow boundaries and the remaining boundaries are constant-head boundaries. The head gradient is assumed to change linearly depending on the direction.

In order to simulate different groundwater flow directions, the head gradient on the boundary in the x-direction and in the z-direction are constant (0.001 and 0 respectively) while the y-direction

148 gradient is 0.004 for simulating regional groundwater directed laterally toward the stream and 0.0005
149 for regional groundwater flowing in the direction of stream flow. These values were selected based
150 on Cardenas (2009a, 2009b). The third groundwater flow scenario assumes groundwater directed
151 south-west diagonally across the stream, with a boundary gradient in the y-direction of 0.0005 in the
152 area north of the stream and 0.0001 south of the stream.

153 The effect of the hydraulic gradient on the x-direction (Figure 1) was tested by comparing
154 results for a low gradient of 0.0005 and a high gradient of 0.01. The effect of the 40 m constant aquifer
155 thickness was tested by modeling aquifer with thicknesses of 5 m and 80 m. Similarly, different
156 stream morphologies were tested by varying the stream width between 2 and 10 m, and the meander
157 wavelength between 30 (S=1.94) and 60 m (S=1.39). The effect of the constant hydraulic
158 conductivity was investigated by varying the hydraulic conductivity between 20 and 80 m/d. These
159 scenarios were simulated for the highly sinuous stream with groundwater flow directed laterally
160 toward the stream.

161 ## 2.2 Grindsted stream field site

162 To examine the implications of findings for real streams with more complex geometries with
163 time varying boundary conditions, a 500 m reach scale numerical model of a field site in southern
164 Jutland, Denmark (Figure 2) was constructed. Grindsted stream has a catchment area of
165 approximately 200 km^2, is 1-2.5 m deep and 8-12 m wide. The unconfined aquifer is 80 m thick and
166 is in hydraulic contact with the stream. The geology is composed of a Quaternary sand formation for
167 the first 10-15 mbgs and, below that, a Tertiary sand formation. The aquifer is underlain by a thick
168 and extensive Tertiary clay layer at 80 mbgs (Barlebo et al., 1998; Heron et al., 1998). Two
169 contaminated sites are present in the surrounding area: Grindsted factory located 1.5 km north of the
170 stream, and Grindsted landfill located 2 km south of the stream (Kjeldsen et al., 1998). From these
171 sites, contaminant plumes discharge into the stream, as evident by examination of stream water

quality (Rasmussen et al., 2016). The domain of the numerical model was designed in order to include the area where the contaminant plumes discharge to the stream. This paper focuses on an assessment of the 3D groundwater flows to the stream. The analysis of the coupled contaminant transport processes is beyond the scope of this paper and will not be discussed further.

The regional equipotential map (Figure 2) was used to define the lateral extent of the model domain and its geometry. Equipotential boundaries, where the flow is perpendicular to the boundary and the head is constant over depth, are employed (Aisopou et al., 2015b). The remaining boundaries are placed along streamlines where a no-flow condition is assumed on vertical sides. The temporal variability of groundwater flow to streams was modelled accounting for variation in precipitation, stream water level and groundwater head. Precipitation data were collected by the Danish Meteorological Institute at a measurement station at Billund Airport, 15 km from the study site (DMI, 2015). The temporal variation in groundwater heads was monitored at several wells in the Grindsted area (selected wells are shown in Figure 2). Well 114.1996 was used to set the variable head on the southern boundary, adjusting all measured heads by 1.2 m because the well is not located exactly on the boundary. Similarly, the head at well 114.1447 was applied on the northern boundary, with an adjustment of 0.9 m. The adjustment was made as part of the model calibration in order to fit the simulated with the observed groundwater head level at the two wells located inside the model domain: 114.1448 and 114.1997. The Quaternary and the tertiary layers are both sandy and have similar hydrogeological properties. Therefore, it was decided to assume a homogenous sandy aquifer. During the model calibration, values of 30 m/d for the horizontal hydraulic conductivity and 3 m/d for the vertical hydraulic conductivity were selected. These values are being similar to the hydraulic conductivities from other field and model studies in the area (Barlebo et al. 1998; Bjerg et al., 1995; Lønborg et al., 2006).

Stream water level data was obtained at the Tingvejen gaging station, located 2.5 km upstream of the model domain, and at Eg Bro, located 8.1 km downstream of the model domain. The average water slope between the two gaging stations is 0.001. The mean annual stream discharge is 2,150 l/s at Tingvejen and 2,980 l/s at Eg Bro. The simulated stream reach is about 900 m long and the annual average groundwater discharge to the stream in the reach, estimated from annual average discharge measurements from the gaging stations, is 70 l/s.

Based on three measured streambed cross sections, the stream cross section is modelled using a half-ellipsoidal with depth of 3 m and width of 10 m. The depth of 3 m is larger than the stream water depth to allow for in stream head variations without overbank flow. The stream is implemented as a time varying head boundary where the head varies linearly along the channel with a gradient of 0.001, corresponding to the average water slope between the two gaging stations. The slope of the streambed is assumed to be 0.001, as to the stream water slope.

2.3 Modeling groundwater flow to streams with the coordinate transformation method

The groundwater head at the interface between groundwater and the streambed which controls the flow to/from the stream is temporally variable and is difficult to simulate with a traditional groundwater flow model employing a regular grid. Two methods have been developed to describe the variability of groundwater head in unconfined aquifers: the moving mesh (Knupp, 1996; Darbandi et al., 2007; Bresciani et al., 2011) and the saturated-unsaturated groundwater flow (Freeze, 1971; Sugio and Desay, 1987; Dogan and Motz, 2005; Keating and Zyvoloski, 2009; Camporese et al., 2010; Walther et al., 2012). A review of studies applying these methods is provided in Table S2. These methods were developed for unconfined aquifers without considering stream interaction, which introduces large local variations in groundwater head.

The moving mesh method solves the groundwater flow problem under saturated conditions and adjusts the mesh depending on the groundwater head calculated at the previous time step. The method

219 requires re-meshing at each time step, which is very computationally demanding (Freeze, 1971;
220 Kinouchi et al., 1991; Knupp 1996) and can fail for large changes in the water head between time
221 steps or for steep gradients, such as at the stream-aquifer interface (Bresciani et al., 2011; COMSOL,
222 2013). The saturated-unsaturated method solves the flow equation in both the saturated and
223 unsaturated zone avoiding the problem of explicitly describing the water table surface (An et al.,
224 2010; Kinouchi et al., 1991). However, the method is more computationally demanding than saturated
225 flow models and is rarely justified when the main focus is the saturated flow (Keating and Zyvoloski,
226 2009).

227 The new coordinate transformation of Boon et al. (2016) was used to solve the groundwater
228 flow equations in the model domain. The method reduces computational time by employing a
229 coordinate transformation so that the saturated groundwater flow equations are solved on a fixed
230 mesh (Figure 3). For comparison purposes, the equations were also solved on a domain with a
231 dynamically deforming mesh, and by a coupled saturated/unsaturated flow solver (Supporting
232 information S1).

233 To test the three methods for the groundwater flow to streams problem, they were implemented
234 for a two-dimensional test case and their computational accuracy and efficiency compared (Section
235 S1 in the supporting information). The comparison between the methods shows (Table S4) that the
236 coordinate transformation method is the least computationally demanding of the three methods for a
237 2-D test problem, requiring 32 times less computational effort than the saturated-unsaturated
238 approach and 3 times less time than moving mesh, for a relatively coarse discretization. Differences
239 become larger in 3-D and when the grid is refined: the computational time required by the moving
240 mesh in a 3-D test (137 min) is 32 times more computational time than the coordinate transformation
241 (4 min). Furthermore, the coordinate transformation method does not lead to instabilities and
242 oscillations, problems that were encountered with the moving mesh. The coordinate transformation

is a much more computationally efficient solution making it possible to simulate a variety of scenarios and properly explore the problem. Thus, the coordinate transformation method is employed for all examples in this study.

In the coordinate transformation method (Boon et al., 2016), the groundwater flow equation for saturated conditions is solved in a transformed domain $\widehat{\Omega}$:

$$S_s \frac{\partial \hat{h}}{\partial t} + \nabla \cdot \left(- \widehat{\mathbf{K}} \cdot \nabla \hat{h} \right) = 0 \qquad \text{in } \widehat{\Omega} \qquad (1)$$

Where Ss is the specific yield [1/m], $\hat{h}$ is the hydraulic head in the transformed space [m] and $\widehat{K}$ is the hydraulic conductivity tensor in the transformed space [m/s]. The groundwater flow velocity in the transformed domain $\widehat{\Omega}$ becomes:

$$\hat{q} = -\widehat{\mathbf{K}} \cdot \nabla \hat{h} \qquad (2)$$

The conditions at the top boundary Γ are:

$$\hat{h}(\hat{x}, t) = \zeta(\hat{x}, t) \qquad \text{on } \Gamma \qquad (3)$$

$$-\mathbf{e_\Gamma} \cdot \left(-\widehat{\mathbf{K}} \cdot \nabla \hat{h} \right) = \left(I - S_y \frac{\partial \zeta}{\partial t} \right) \qquad \text{on } \Gamma \qquad (4)$$

where S_y is the specific yield [-],ζ is the elevation for the free surface [-], and e_Γ is the unit normal to Γ. The governing equations are solved in Comsol Multiphysics, which employs a finite element numerical approximation (COMSOL, 2013). The finite element method employs the weak form of (1) with a linear polynomial Lagrange test function $g \in H^1(\widehat{\Omega})$ which is combined with the boundary equation (4) and input into COMSOL Multiphysics:

$$\left(S_s \frac{\partial \hat{h}}{\partial t} + \nabla \cdot \left(- \widehat{\mathbf{K}} \cdot \nabla \hat{h} \right), g \right)_{\widehat{\Omega}}$$

$$= \left(S_s \frac{\partial \hat{h}}{\partial t}, g \right)_{\widehat{\Omega}} + \left(\widehat{\mathbf{K}} \cdot \nabla \hat{h}, \nabla g \right)_{\widehat{\Omega}} + \left(\mathbf{e} \cdot \left(-\widehat{\mathbf{K}} \cdot \nabla \hat{h} \right), g \right)_{\Gamma}$$

$$= \left(S_s \frac{\partial \hat{h}}{\partial t}, g \right)_{\hat{\Omega}} + \left(\hat{\mathbf{K}} \cdot \nabla \hat{h}, \nabla g \right)_{\hat{\Omega}} - \left(\left(I - S_y \frac{\partial \zeta}{\partial t} \right) e_{\Gamma_z}, g \right)_{\Gamma} = 0 \quad (5)$$

The linear transformation ψ is:

$$\mathbf{x} = \psi(\hat{x}, \hat{z}, t) = [\hat{x}, 0] + \zeta(\hat{x}, t)\hat{z}\mathbf{e_z} \quad (6)$$

$$h(x, z, t) = \hat{h}(\hat{x}, \hat{z}, t) \quad (7)$$

where e_z is the unit vector in the z-direction. The hydraulic conductivity field is a function of the elevation of the free surface ζ and can be derived from the linear transformation:

$$\hat{\mathbf{K}}(\hat{x}, \hat{z}, t) = \det \hat{\nabla}\psi \, (\hat{\nabla}\psi)^{-1} \mathbf{K} (\hat{\nabla}^T \psi)^{-1}$$

$$= \zeta \begin{bmatrix} K_h & -K_h \hat{z} \zeta^{-1} \hat{\nabla}\zeta \\ -K_h \hat{z} \zeta^{-1} \hat{\nabla}^T \zeta & \left(K_h \hat{z}^2 \hat{\nabla}^T \zeta \hat{\nabla} \zeta + K_v \right) \zeta^{-2} \end{bmatrix} \quad (8)$$

In equation (8) $\zeta = \zeta(\hat{x}, t)$, $K_h = K_h(x, z)$, $K_v = K_v(x, z)$, and $\hat{K}$ depends on the linear transformation described in equation (6) and (7).

Apart from the boundary condition for the top boundary (5), the boundary conditions applied in the transformed domain are: no-flow for the bottom boundary, and time-variable fixed-head for the lateral boundaries. The transform formulation, as well as its numerical implementation using lowest-order Lagrange finite elements is provably stable and convergent (Boon et al., 2016).

3. Results

In this section, the effect of meander bends on groundwater flow to streams is presented, with focus on both the vertical and horizontal variability of groundwater flow patterns. The difference between the vertical and horizontal flow could neither have been observed, nor investigated, with a 2-D model. First, the effect of sinuosity is analyzed in combination with other parameters affecting groundwater flow to streams through the synthetic sinuous stream model; then, the results from the Grindsted stream field site are described.

3.1 Horizontal variability of the groundwater flow to the stream

The groundwater discharge to the stream at the upper edge of the stream-aquifer interface is shown in Figure 4, where the red arrows are proportional to the horizontal groundwater discharge. Table 1 shows the mean flux over one meander from both stream sides (m/s) for each scenario and the percentage of flow discharged at the outward pointing side of the meander and at the inward pointing side of the meander.

The straight stream has a constant discharge along the stream for all hydraulic gradients (Figure 4a, 4b, and 4c), except at the boundaries, where the boundary conditions affected the results. In the moderately sinuous stream (Figure 4d, 4e, and 4f), the groundwater discharge to the stream is not constant and changes depending on the location along the stream meander, as shown by the arrow size. The discharge is largest at the extremes of the stream meanders, with 68% and 67% of the groundwater flux entering the stream on the outward pointing side of the meanders for a J_{yx} (ratio between the hydraulic gradient in the y-direction and in the x-direction) of 4 and 0.5 respectively (Table 1). This variation in the groundwater discharge to the stream is due to the stream sinuosity and increases with the sinuosity: 85% and 82% of the groundwater flux enters at the outward pointing side of the meander for a J_{yx} of 4 and 0.5 respectively (corresponding to Figure 4g and 4h). This effect can also be seen by comparing Figure 4d and 4e with Figure 4g, 4h.

The ratio between the hydraulic gradient in the y and x-direction (J_{yx}) and, thus, the hydraulic gradient in the y-direction affect the groundwater direction to the stream. In the straight stream, for a large J_{yx} (Figure 4a), the groundwater direction is more perpendicular to the stream (compared with a lower J_{yx} in Figure 4b). When two different values of J_{yx} are applied on each side of the stream (Figure 4c), both the direction of groundwater to the stream and the magnitude of the discharge changes on each side of the stream. A lower value of J_{yx} corresponds to a lower groundwater discharge to the stream, as shown on the southern part of the stream in Figure 4c. Therefore, the percentage of

297 groundwater flux to the stream is lower (39%) on the southern side of the stream, where the hydraulic
298 gradient in the y-direction is higher, compared to northern side where the gradient in the y-direction
299 is lower (61%).

300 The effect of the hydraulic gradient can also be observed in the moderately (Figure 4f) and
301 highly sinuous stream (Figure 4i). The highest groundwater flow to the stream is located further
302 upstream on the outward pointing side of the meander bend when decreasing the value of J_{yx}.
303 Therefore, the groundwater flux on the outward pointing side increases from 67% to 74% for the
304 moderately sinuous stream, when the flux is measured on the meander pointing north, where the
305 gradient in the y-direction is higher. The effect of the gradient decreases when the sinuosity increases:
306 for the highly sinuous stream the flux increases from 82% to 84%.

307 **Table 1: Mean groundwater fluxes to the stream at a meander and percentage of the fluxes entering the stream on the outward**
308 **pointing side and on the inward pointing side of the meander. The mean flux was calculated as the integral of the discharge**
309 **along the meander at the stream-aquifer interface divided by the interface area.**

Model	Sinuosity	Meander side	$J_{yx} = 4$	$J_{yx} = 0.5$	$J_{yx}^{north} = 0.5$ $J_{yx}^{south} = 0.1$
Straight stream	1	Northern side [%]	50	50	61
		Southern side [%]	50	50	39
		Mean flux [m/s]	0.58	0.06	0.04
Moderately sinuous stream	1.14	Outward side [%]	68	67	74
		Inward side [%]	32	33	26
		Mean flux [m/s]	0.51	0.06	0.05
Highly sinuous stream	1.74	Outward side [%]	85	82	84
		Inward side [%]	15	18	16
		Mean flux [m/s]	0.48	0.05	0.05

310

311 The results shown in Figure 4 and Table 1 are based on simulations where all parameters are
312 fixed, except for the amplitude of a meander which affects the stream sinuosity, and the ratio between
313 the hydraulic gradient in the y and x-direction. The fixed parameters include the wavelength of a
314 meander (40 m), the hydraulic gradient in the x-direction (1‰), the stream width (5 m), homogenous
315 hydraulic conductivity (40 m/d), and the aquifer depth (40 m). In order to study how these model

316 parameters affect the results shown in Table 1 and Figure 4, the parameters were varied for the
317 scenario with the highly sinuous stream and J_{yx} of 4. The results are summarized in Table 2 and Figure
318 S3 (Supporting Information), with bold values indicating the parameter values used for the
319 simulations in Table 1 and Figure 4.

320 The mean groundwater flux to a stream meander increases with the hydraulic gradient in the x-
321 direction and with the hydraulic conductivity, as described by Darcy's law: from 0.24 m/s to 4.84 m/s
322 for a hydraulic gradient of 0.5‰ and 10‰ respectively, and from 0.25 m/s to 0.94 m/s for
323 conductivities of 20 m/d and 80 m/d respectively. However, the percentages of groundwater entering
324 the stream on one side or the other of the meander do not change. This indicates that the magnitude
325 of the hydraulic gradient and of hydraulic conductivity affect the magnitude of groundwater flow
326 entering the stream, but not the direction of the groundwater flow to the stream.

327 The mean groundwater flux to a stream decreases when increasing the stream width, from 0.53
328 m/s to 0.42 m/s for, respectively, a 2 m and an 8 m wide stream, because the same discharge enters
329 through a larger area for a larger stream. The percentage of groundwater flux entering the stream on
330 the outward pointing side of the meanders is lower (79%) for a 2 m wide stream, compared to an 8 m
331 wide stream (88%). In a wider stream, the stream bank on the outward pointing side is closer to the
332 model boundary conditions, leading to a steeper hydraulic gradient and a higher groundwater flux to
333 the stream. Even though the stream width affects the magnitude of the groundwater flux to the stream,
334 it does not affect the direction of groundwater flow to the stream (see Supporting Information, Figure
335 S3).

336 The wavelength of the stream meanders affects both the average discharge to the stream and
337 the percentage of groundwater entering on each side of a meander bend. The average discharge to the
338 stream is 0.44 m/s for the scenario with the wavelength of 30 m, and 0.55 m/s with the wavelength
339 of 60 m. The groundwater flux on the outward pointing side of a meander decreases, from 89% to

75%, by increasing the wavelength from 30 to 60 m. When the amplitude of a meander is held constant and the wavelength increases, the sinuosity of the stream decreases. Thus, the flow to the stream is also dependent on sinuosity.

The average groundwater flux increases with increasing the aquifer thickness: from 0.12 m/s to 0.64 m/s for an aquifer thickness of 5 m and 80 m respectively. This can be explained by looking at the depth of the origin of groundwater, discharging to the stream, compared to the depth of the origin of groundwater exiting the model at the downstream boundaries (as seen in Section 3.2 and Figure 6). The percentage of water entering the stream on the outward pointing side of a meander is also affected and decreases from 99% for the 5 m thick aquifer to 83% for the 80 m thick aquifer.

Based on the model sensitivity analysis, the parameters most strongly affecting the spatial distribution of the groundwater flow to a stream are the groundwater flow direction, the stream sinuosity, and the aquifer thickness. The effect of these parameters is further analyzed in Section 3.2 where the groundwater flow to the stream in a vertical cross section is examined.

Table 1: Groundwater discharge to the stream at a meander bend. The base parameter values, shown in bold, are the same as those used for the simulation, whose results are summarized in Figure 4, Figure 5, and Table 1. Each parameter is then varied and results shown. The ratio between the hydraulic gradient in the y- and x-direction (J_{yx} = 4) and the meander amplitude (α = 13.5) were fixed for these simulations.

		Wavelength [m]			**Hydraulic gradient in x-direction [‰]**			**Stream width [m]**			**Hydraulic conductivity [m/d]**			**Aquifer thickness [m]**		
		30	**40**	60	0.5	**1**	10	2	**5**	8	20	**40**	80	5	**40**	80
	Sinuosity	1.94	**1.74**	1.39	1.74	**1.74**	1.74	1.74	**1.74**	1.74	1.74	**1.74**	1.74	1.74	**1.74**	1.74
Meander side	**Outward side [%]**	89	**85**	75	85	**85**	86	79	**85**	88	85	**85**	87	99	**85**	83
	Inward side [%]	11	**15**	25	15	**15**	14	21	**15**	12	15	**15**	13	1	**15**	17
	Mean flux [m/s]	0.44	**0.48**	0.55	0.24	**0.48**	4.84	0.53	**0.48**	0.42	0.25	**0.48**	0.94	0.12	**0.48**	0.64

3.2 Vertical variability of the groundwater flow to the stream

In order to analyze the vertical spatial variability of the groundwater close to the stream, the groundwater flow direction on a vertical cross section perpendicular to the stream is shown in Figure 6 with particle tracks to highlight the streamlines: blue for the particles originating south of the stream and red for particles originating from the north. The contour lines (black lines) show the equipotential lines separated by 0.005 m interval.

In the straight stream (Figure 5a and 5b), the groundwater streamlines enter the stream through the stream bank closest to the boundary of streamline origin. In Figure 5c, the hydraulic gradient in the y-direction is larger on the northern side of the stream compared to the southern side. Here, the groundwater streamlines originating from the north enter the stream on both the northern and southern side of the stream, with the discharging bank depending on the depth of origin of the groundwater flow.

In the moderately sinuous stream and in the highly sinuous stream, the cross section was placed at a point with a meander pointing south. When the hydraulic gradient in the y-direction is the same on both sides of the stream (moderately sinuous stream: Figure 5d and 5e; highly sinuous stream: Figure 5g and 5h), the groundwater streamlines originating from the south enter the stream on both the southern and northern side of the stream, with the discharging bank depending on the depth of the groundwater flow. This effect increases with the stream sinuosity, as can be observed by comparing Figure 5d and 5g. Furthermore, a similar, but reversed situation occurs in Figure 5c, where flow patterns are driven by the difference in hydraulic gradient in the y-direction.

In Figure 5f and 5i, the effects of stream sinuosity and a change in the flow direction at the stream are combined. The two factors have an opposing effect on results; thus, the combined effect is smoothed (compare Figure 5c, 5f, and 5i). In contrast, at meander bends pointing to the north, the effects of the meander bend and the changes in hydraulic gradient reinforce each other.

385 The effect of the aquifer thickness on the groundwater flow to a stream is shown in Figure 6 for
386 the highly sinuous stream with J_{yx} of 4. In the shallow aquifer, which is 5 m thick, all groundwater
387 discharges to the stream. However, for the 40 m thick aquifer, groundwater in the top 32 m discharges
388 to the stream, while the deepest groundwater, in the lowest 8 m of the aquifer, flows horizontally
389 beneath the stream and is not affected by the stream. Increasing the thickness of the aquifer, from 5
390 m to 40 m, results in an increase from 0.12 to 0.48 m/s of the average groundwater flux to the stream,
391 as observed in Table 2. When further increasing the aquifer thickness to 80 m, groundwater in the
392 deepest 32 m of the aquifer flows horizontally downstream without entering the stream, as shown by
393 the horizontal groundwater flow paths in the plan view section 60 mbgs (Figure 6d). The horizontal
394 hydraulic gradient is affected by the stream in the deepest part of the aquifer, while the vertical
395 gradient is not. This indicates that streams have a diminishing effect on groundwater discharge as
396 aquifer thickness increases. Moreover, the area discharging to the stream does not linearly increase
397 with the aquifer thickness. These results are based on three scenarios where the aquifer depth is varied
398 and the stream depth is assumed to be constant. The effect of the stream depth is likely to combine
399 with effect of the aquifer depth, when both parameters are varied. However, this is beyond the scope
400 of this analysis.
401 The groundwater flow component in the y-direction is shown in Figure 7. The figure shows two
402 cross section: one follows the path to the stream (Figure 7a, 7c, and 7e) while the other is centered in
403 the middle of the model domain (Figure 7b, 7d, and 7f). The results are shown for the straight, the
404 moderately, and the highly sinuous stream scenarios with a constant J_{yx} of 0.5. The green color
405 indicates the absence of flow in the y-direction, the blue color indicates a negative flow, directed to
406 the south, and the red color indicates a positive flow, directed to the north.
407 On the cross section following the stream, the straight stream (Figure 7) shows that y-directional
408 groundwater flow below the stream is zero. The results are presented only for a constant J_{yx} of 0.5

409 and a constant aquifer thickness of 40 m, but are valid whenever the hydraulic gradient and the aquifer
410 thickness is constant. The scenario with different hydraulic gradients in the y-direction at the two
411 sides of the stream shows groundwater flow below the stream from north to south, as shown in Figure
412 7c.

413 The moderately sinuous stream (Figure 7c) shows areas colored in blue, associated with a
414 meander pointing toward north, and the areas colored in red, with a meander pointing south. For
415 meanders pointing north, groundwater from the northern side of the stream flows beneath the stream
416 in a southerly direction (the flow has a negative sign), while for meanders pointing south, groundwater
417 from the southern side of the stream flows beneath the stream in a northerly direction (the flow has a
418 positive sign). Between two meander extremes, an area with no flow in the y direction occurs (Figure
419 7c). Y-directional groundwater flow under the stream is greatest for shallow depths and decreases
420 deeper in the aquifer. The same pattern in the groundwater flows can be observed for the highly
421 sinuous stream (Figure 7e), but is more pronounced than for the moderately sinuous stream.

422 The groundwater flow between the northern and southern side of the stream is further analyzed
423 by showing the y-direction flow on a vertical cross section centered in the middle of the model domain
424 (Figure 7b, 7d, and 7f). Curiously, Figure 7d show that the greatest amount of groundwater flow
425 across the stream centerline occurs for the moderately sinuous stream. When sinuosity increases there
426 is less flow inside the meander bend (Figure 4), and a lower y-directional flow across the stream
427 centerline (Figure 7e). This effect is related to the higher discharge to the outward pointing side of a
428 meander bend in the highly sinuous stream, compared to the moderately sinuous stream. In the highly
429 sinuous stream more water enters the stream at the meander bend, instead of crossing the line placed
430 in the middle of the model domain and entering the stream in the inward pointing side of the meander.

3.3 Grindsted stream field site

The model implemented at the Grindsted stream field site was first evaluated by comparing model results with the observed groundwater head and discharge to the stream. In Figure 8, the simulated groundwater head is compared to the observed head at wells located within the model domain: 114.1448 and 114.1997 (Figure 2). In well 114.1448, the model describes the variation groundwater head well, except for the period May-July 2014 when the simulated head (red line) is higher than the observed (black dots). In well 114.1997, the meandering stream model properly simulates the head until June 2014, but the head is overestimated for the remaining simulation time. This is confirmed by the Nash-Sutcliffe efficiency coefficient (Nash and Sutcliffe, 1970) for the entire simulation period of 0.63 and 0.68 at the two observation wells 114.1448 and 114.1997 respectively. The simulated annual average groundwater discharge to the stream is 75 l/s, which matches well the annual averaged discharge estimated from the gaging stations (70 l/s). The inflow at the upgradient groundwater boundaries resembles the discharge to the stream, with small differences due to changes in storage in the domain and recharge.

The simulated groundwater discharge to the stream along the entire modeled stream stretch is shown in Figure 8 (green line). The groundwater discharge to the stream varies up to 40% during the one year simulation. Despite this, the spatial patterns of the groundwater flow to the stream in the simulations are not time varying. This is because the modeled stream is always a gaining stream, and head variations are small (up to 0.4 m over a one year simulation) compared to the aquifer thickness (80 m). We carefully note, however, that the spatial patterns of groundwater flow to the stream will probably change with time for a stream that switches between being gaining and losing conditions.

The horizontal groundwater flow at the upper edge of the stream-aquifer interface is shown in Figure 9 by the red arrows, whose length is proportionate to the magnitude of the flow. The groundwater discharge is not constant, but changes depending on the location along the stream. As

for the sinusoidal stream geometries (Figure 4), the groundwater discharge peaks at the outside extremes of the meander bends and is smallest on the inside of the meander bends.

The groundwater flow to the stream at two vertical cross sections perpendicular to the stream is shown in Figure 10. The cross section in Figure 10a is placed at the location of a meander bend pointing to the north and the cross section in Figure 10b is placed where a meander bend is pointing to the south. In Figure 10a, the particles originating in the shallow part of the aquifer north from the stream enter the stream at the northern bank. The particles originating in the deep part of the aquifer north of the stream enter the stream on the southern bank while the particles coming from the southern side of the aquifer enter the stream on the shallow part of the southern bank. The reverse pattern is observed in Figure 10b. This is similar to the results of the moderately sinuous stream (Figure 5d and 5e) and the high sinuous stream (Figure 5g and 5h).

4. Discussion

This study shows that meander bends lead to significant spatial variability in groundwater flow to streams. The results show that most of groundwater flowing to the stream enters the stream at the outward pointing side of the meander bend (85% for the highly sinuous stream with a J_{yx} of 4), just upstream of the extremities of the meander (Figure 4 for the synthetic stream and Figure 9 for Grindsted stream). The groundwater discharge to the stream is lowest on the inside of meander bends, where only 15% of groundwater enters the stream for the highly sinuous stream with a J_{yx} of 4. The amount of groundwater entering the stream is affected by the groundwater flow direction in the aquifer. In case of regional groundwater flowing perpendicularly to the stream direction, 85% of groundwater discharge occurs on the outward pointing side of a meander, compared to 82% for regional groundwater flowing in the direction of the stream. In this case, the largest groundwater flows occur on the upstream part of the outward pointing meander. For real streams, such as the

478 Grindsted stream (Figure 9) the variations in the groundwater discharge at the stream-aquifer interface
479 are not as regular as for the synthetic streams (Figure 4). In the synthetic streams, all meanders have
480 the same amplitude and period and are oriented in the same way relative to the groundwater flow
481 direction. In the Grindsted stream, the meanders have different size and are oriented differently. Thus,
482 the spatial variability of the groundwater flow to streams is affected by the size as well as by the
483 orientation of the meander bend.

484 In the field study of Weatherill et al. (2014), a high concentration of contaminants in
485 groundwater discharge was detected at the outside of a meander bend. Our study, which indicates that
486 the outward pointing side of the bends is the dominant location for groundwater discharge, helps
487 explain those results.

488 The groundwater flow to the stream is observed to vary greatly with depth for both the synthetic
489 (Figure 5, 6, and 7) and Grindsted streams (Figure 10). This confirms that groundwater flow to
490 streams at meandering streams is three dimensional, as previously suggested by Harvey and Bencala
491 (1993), Modica et al. (1998), and Flipo et al. (2014). The present study investigates how the vertical
492 variability of the groundwater flow to the stream is affected by the meander bends with the
493 discharging bank being dependent on the depth of origin of the groundwater and the stream geometry.
494 The amount of groundwater entering the stream on the opposite bank, increases with the sinuosity
495 (Figure 7a and 7b) and amplitude of the meanders (Figure 5). Curiously the magnitude of the flow
496 crossing the stream center line is highest for moderately sinuous streams and decreases when
497 increasing the sinuosity (Figure 7d and 7e). Groundwater can enter the stream on the opposite bank
498 from its origin because of difference in hydraulic gradient in the aquifer between the two sides of the
499 stream, as occurring when the regional groundwater flow direction is across the stream. The regional
500 groundwater flow can either enhance or smooth the effect of the stream sinuosity, depending on the
501 direction of the regional groundwater flow and the orientation of the meander bends.

The observation that groundwater can flow below a stream and enter the stream through the opposite bank has previously been described by Aisopou et al. (2015a) and Miracapillo and Morel-Seytoux (2014). However, the factors causing groundwater to enter the stream through the opposite bank are different in those papers than here. In Aisopou et al. (2015a), the presence of a pumping well on one side of the stream creates a head gradient that forces groundwater to cross to the opposite side of the stream and enter the stream at the bank closest to the well. In Miracapillo and Morel-Seytoux (2014), the difference of the horizontal gradient between the two sides of the stream imposed by the boundary conditions, is responsible for the flow below the stream. Here we focus on the combined influence of stream geometry and groundwater flow direction on the location of groundwater discharge to a stream.

The synthetic stream and the Grindsted stream models have been implemented using different boundary conditions. In the synthetic stream, all the lateral boundary conditions (Figure 1) are constant head and account for the head gradient in the x and y direction. In the Grindsted stream model (Figure 2), the boundaries perpendicular to the stream are streamlines (no-flow boundaries) and the upstream groundwater boundaries are fixed-head. The constant head boundaries of the synthetic stream model assume no vertical groundwater gradients. As previously discussed, this is not the case close to a meandering stream. The streamline boundaries applied in the Grindsted stream model allow a vertical gradient. However, the streamline boundaries of the Grindsted model do not allow a horizontal flow across the stream lines in the aquifer. Thus along-stream groundwater flow is better modeled by constant head boundaries. Neither the no-flow nor the constant head boundary conditions perfectly describe conditions under streams. However, this paper has shown that the effect of meanders is similar for both types of groundwater boundary conditions (compare the sinusoidal examples with fixed head boundaries with the Grindsted model with the no flow boundaries). In addition, the results from a larger modeling domain (Figure S4) show that the effect of stream

meanders on the groundwater flow pattern to the stream do not change when the model boundaries are further from the stream (compare Figure 5i with Figure S4), so the conclusions are robust despite boundary condition uncertainty.

The hydraulic conductivity distribution in the aquifer and in the stream bed is one of the factors, together with the stream morphology and the hydraulic gradient, known to affect the groundwater flow to streams. Recent studies by Krause et al. (2012), Brookfield and Sudicky (2013), Gomez-Velez et al. (2014), and Poulsen et al. (2015) have focused on the effect of the hydraulic conductivity distribution on the groundwater discharge to streams. Since the aim of this study is to investigate the effect of stream meanders and groundwater flow direction on the groundwater flow to streams at the reach scale, the models assume a homogenous sandy aquifer and a constant stream hydraulic gradient. Future studies that investigate the combined effect of stream meanders, varying stream-aquifer hydraulic gradients, and heterogeneous aquifer systems (spatially varying hydraulic conductivity distributions) or layered aquifers would enhance the understanding on groundwater flow to streams.

5. Conclusions

A numerical modeling study analyzing the effect of meander bends on the spatial variability of the groundwater flow in an unconfined and homogenous sandy aquifer to a gaining stream at the reach scale is presented. Results were obtained by applying the coordinate transformation method of Boon et al. (2016) to a new problem: the groundwater flow to streams.

The results showed that presence of meander bends leads to significant spatial variability in groundwater discharge to streams. The groundwater fluxes are highest at the meander bend extremes, up to 85% of the mean fluxes to a meander with a sinuosity of 1.74, and much lower on the inside of meander bends. This effect increases with the stream sinuosity. The magnitude of the hydraulic gradient of groundwater and of the hydraulic conductivity in the aquifer affects the mean groundwater

549 flux to the stream, while the stream width and the direction of groundwater affects the groundwater
550 flow direction to the stream. Groundwater gradients combine with the effect of stream meanders and
551 can either enhance or smooth the effect of a meander bend, depending on groundwater flow
552 directions.

553 The location of the discharge of groundwater along the stream cross section is affected by the
554 stream sinuosity, the direction of the groundwater flow, and the aquifer thickness. At the meander
555 extremes, groundwater coming from the shallow part of the aquifer enters the stream at the outward
556 pointing bank. Groundwater originating from the deep part of the aquifer often flows beneath the
557 stream and enters the stream at the opposite bank at the inward side of a meander bend, with the
558 amount of groundwater flow under the stream increasing with aquifer thickness.

559 The field site application confirmed the finding of the synthetic study case and showed that the
560 irregular geometry of the stream meanders affects the groundwater discharge to the stream. This study
561 improved our conceptual understanding of the groundwater flow paths to meandering streams in an
562 unconfined homogenous sandy aquifer and shows how stream meanders, combined with groundwater
563 flow direction, affect the spatial variability of the groundwater flow to streams at the reach scale in
564 both synthetic and field systems.

565 ## Acknowledgements

566 This study was supported by the research project GEOCON, Advancing GEOlogical,
567 geophysical and CONtaminant monitoring technologies for contaminated site investigation (contract
568 1305-00004B). The funding for GEOCON is provided by Innovation Fund Denmark. Additionally,
569 this study was supported by Norwegian Research Council grant 233736. The data used in this paper
570 can be accessed by contacting the first author Nicola Balbarini at nbal@env.dtu.dk. The authors
571 would like to thanks Vinni Rønde, Anne Thobo Sonne and Ursula McKnight for the field data
572 collection and their valuable assistance in the data interpretation.

References

Aisopou, A., P. J. Binning, H. Albrechtsen and P. L. Bjerg (2015a), Modeling the factors impacting pesticides concentrations in groundwater wells, Groundwater, 53, 5, 722-736 doi: 10.1111/gwat.12264.

Aisopou, A., P. L. Bjerg, A. T. Sonne, N. Balbarini, L. Rosenberg and P. J. Binning (2015b), Dilution and volatilization of groundwater contaminant discharges in streams, Journal of Contaminant Hydrology, doi:10.1016/j.jconhyd.2014.11.004.

An, H., Y. Ichikawa, Y. Tachikawa, and M. Shiiba (2010), Three-dimensional finite difference saturated-unsaturated flow modeling with nonorthogonal grids using a coordinate transformation method, Water Resources Research, 46, W11521, doi:10.1029/2009WR009024.

Anibas, C., B. Verbeiren, K. Buis, J. Chorma´nski, L. De Doncker, T. Okruszko, P. Meire and O. Batelaan (2012), A hierarchical approach on groundwater-surface water interaction in wetlands along the upper Biebrza River, Poland, Hydrology and Earth System Sciences, Vol. 16, Pages 2329-2346, doi: 10.5194/hess-16-2329-2012.

Barlebo, H. C., M. C. Hill, D. Rosbjerg and K. H. Jensen (1998), Concentration Data and Dimensionality in Groundwater Models: Evaluation Using Inverse Modelling, Nordic Hydrology, 29, 149-178.

Binley, A., S. Ullah, A. L. Heathwaite, C. Heppell, P. Byrne, K. Lansdown, M. Trimmer and H. Zhang (2013), Revealing the spatial variability of water fluxes at the groundwater-surface water interface, Water Resources Research, Vol. 49, Pages, 3978-3992, doi:10.1002/wrer.20214.

Bjerg, P.L.; Rügge, K.; Pedersen, J.K.; Christensen, T.H. (1995): Distribution of redox sensitive groundwater quality parameters downgradient of a landfill (Grindsted, Denmark). Environmental Science & Technology, 29, 1387-1394.

Boano F; Camporeale C; Revelli R; Ridolfi L. (2006) Sinuosity-driven hyporheic exchange in meandering rivers, Geophys. Res. Lett., 33, L18406.

Boano, F., R. Revelli, and L. Ridolfi (2009), Quantifying the impact of groundwater discharge on the surface-subsurface exchange, Hydrological Processes, 23, 2108-2126, doi:10.1002/hyp.7278.

Boano, F., C. Camporale and R. Revelli (2010), A linear mode for the coupled surface-subsurface flow in a meandering stream, Water Resources Research, Vol. 46, W07535, doi:10.1029/2009WR008317.

Boano, F., J. W. Harvey, A. marion, A. I. Packman, R. Revelli, L. Ridolfi and A. Wörman (2014), Hyporheic flow and transport processes: Mechanisms, models, and biogeochemical implications, Review of Geophysics, Vol. 52, Pages, 603-679, doi:10.1002/2012RG000417.

Boon, W. M., N. Balbarini, P. J. Binning, and J. M. Nordbotten (2016), Efficient Water Table Evolution Discretization Using Domain Transformation, Computational Geoscience, doi:10.1007/s10596-016-9591-2.

610 Bresciani, E., P. Davy, and J. R. De Dreuzy (2011), A finite volume approach with local adaptation
611 scheme for the simulation of free surface flow in porous media, Int. J. Numer. Anal. Methods
612 Geomech., doi: 10.1002/nag.1065

613 Brookfield, A. E. and E. A. Sudicky (2013), Implications of hyporheic flow on temperature-based
614 estimates of groundwater/surface water interactions, Journal of Hydrologic Engineering,
615 18(10), pp. 1250-1261.

616 Byrne, P., A. Binley, A. L. Heathwaite, S. Ullah, C. M. Heppel, K. Lansdown, H. Zhang, M. Trimmer
617 and P. Keenan (2014), Control of river stage on the reactive chemistry of hyporheic zone,
618 Hydrological processes, 28, 4766-4779, doi: 10.1002/hyp.9981.

619 Camporese, M., C. Paniconi, M. Putti and S. Orlandini (2010), Surface-subsurface flow modeling
620 with path-based runoff routing, boundary condition-based coupling, and assimilation of
621 multisource observation data, Water Resources Research, Vol. 46,
622 doi:10.1029/2008WR007536.

623 Cardenas, M. B., J. L. Wilson and V. A. Zlotnik (2004), Impact of heterogeneity, be forms, and stream
624 curvature on subchannel hyporheic exchange, Water Resources Research, Vol. 40, W08307,
625 doi:10..1029/2004WR003008.

626 Cardenas, M. B. (2008), The effect of river bend morphology on flow and timescales of surface-
627 groundwater exchange across pointbars, Journal of Hydrology, 362, 134-141,
628 doi:10.1016/j.hydrol.2008.08.018.

629 Cardenas, M. B. (2009a), Stream-aquifer interactions and hyporheic exchange gaining and losing
630 sinuous streams, Water Resources Research, Vol. 45, W06429, doi:10.1029/2008WR007651

631 Cardenas, M. B. (2009b), A model for lateral hyporheic flow based on valley slope and channel
632 sinuosity, Water Resources Research, Vol. 45, W01501, doi:10.1029/2008WR007442.

633 Cey, E. E., D. L. Rudolph, G. W. Parkin and R. Aravena (1998), Quantifying groundwater discharge
634 to a small perennial stream in southern Ontario, Canada, Journal of Hydrology, Vol. 210, Pages
635 21-37.

636 COMSOL (2013), COMSOL Multiphysics Reference Manual, Version 4.4.

637 Conant Jr., B., J. A. Cherry, and R. W. Gillham (2004), A PCE groundwater plume discharging to a
638 river: influence of the streambed and near-river zone on contaminant distributions, Journal of
639 Contaminant Hydrology, 73, 249-279, doi:10.1016/j.jconhyd.2004.04.001.

640 Dahl, M., B. Nilsson, J. H. Langhoff and J. C. Refsgaard (2007), Review of classification systems
641 and new multi-scale typology of groundwater-surface water interaction, Journal of Hydrology,
642 Vol. 344, Pages 1-16, doi:10.1016/j.jhydrol.2007.06.027.

643 Darbandi, M., S.O. Torabi, M. Saadat, Y. Daghighi, D. Jarrahbashi (2007), A Moving Mesh Finite-
644 Volume Method to Solve Free-Surface Seepage Problem in Arbitrary Geometries, International
645 Journal for Numerical and Analytical Methods in Geomechanics, Vol. 31, Pages 1609-1629.

646 Derx, J., A. P. Blaschke and G. Blöschl (2010), Three dimensional flow pattern at the river-aquifer
647 interface-a case study at the Danube, Advances in Water Resources, Vol. 33, Pages 1375-1387.

648 Diem, S., P. Renard and M. Schirmer (2014), Assessing the effect of different river water level
649 interpolations schemes on modeled groundwater residence times, Journal of Hydrology, Vol.
650 51, Pages 393-402, doi:10.1016/j.jhydrol.2013.12.049.

651 DMI (2015), Available from: <http://www.dmi.dk/vejr/> [20 December 2015].

652 Dogan A. and L. H. Motz (2005), Saturated-unsaturated 3D groundwater model. I: Development,
653 Journal of Hydrologic Engineering, DOI: 10.1061/(ASCE)1084-0699(2005)10:6(492).

654 Fernando, H. J. S. (2013), Handbook of environmental fluid dynamics, CRC Press, Volume 2,
655 Chapter 2, Pages 19-30.

656 Flipo, N., A. Mouhri, B. Labarthe, S. Biancamaria, A. Riviere and P. Weill (2014), Continental
657 hydrosystem modelling: the concept of nested stream-aquifer interfaces, Hydrology and Earth
658 System Sciences, Vol. 18, Pages 3121-3149, doi: 10.5194/hess-18-3121-2014.

659 Freeze, R. A. (1971), Three-Dimensional, Transient, Saturated-Unsaturated Flow in a Groundwater
660 Basin, Water Resources Research, Vol. 7, Pages 347-366, doi:10.1029/WR007i002p00347.

661 Freitas, J. G., M. O. Rivett, R. S. Roche, M. Durrant, C. Walker and J. H. Tellam (2015),
662 Heterogeneous hyporheic zone dechlorination of a TCE groundwater plume discharging to an
663 urban river reach, Science of the Total Environment, Vol 505, Pages 236-252.

664 Gomez-Velez, J. D., S. Krause, and J. L. Wilson (2014), Effect of low-permeability layers on spatial
665 patterns of hyporheic exchange and groundwater upwelling, Water Resources Research,
666 doi:10.1002/2013WR015054.

667 Gomez-Velez, J.D., J.W. Harvey, M.B. Cardenas, and B. Kiel (2015), Denitrification in the
668 Mississippi River network controlled by flow through river bedforms, Nature Geoscience, doi:
669 10.1038/NGEO2567.

670 Guay, C., M. Nastev, C. Paniconi and M. Sulis (2013), Comparison of two modeling approaches for
671 groundwater-surface water interactions, Hydrological Processes, Vol. 27, Pages 2258-2270.

672 Harvey, J. W. and K. E. Bencala (1993), The Effect of Streambed Topography on Surface-Subsurface
673 Water Exchange in Mountain Catchments, Water Resources Research, Vol. 29, No. 1, Pages
674 89-98.

675 Heron,G., Bjerg,P.L., Gravesen,P., Ludvigsen,L. & Christensen,T.H. (1998): Geology and sediment
676 geochemistry of a landfill leachate contaminated aquifer (Grindsted, Denmark). Journal of
677 Contaminant Hydrology, **29**, 301-317.

678 Karan, S., P. Engesgaard, M. C. Looms, T. Laier and J. Kazmierczak (2013), Groundwater flow and
679 mixing in a wetland-stream system: Field study and numerical modeling, Journal of Hydrology,
680 Vol. 488, Pages 73-83.

681 Keating, E. and G. Zyvoloski (2009), Saturated-unsaturated 3D groundwater model. I: Development,
682 Ground Water, Vol. 4, Pages 569.579, doi: 10.1111/j.1745-6584.2009.00555.x.

683 Kinouchi, T., M. Kanda and M. Hino (1991), Numerical simulation of infiltration and solute transport
684 in an S-shaped model basin by a boundary-fitted grid system, Journal of Hydrology, Vol. 122,
685 Pages 373-406, doi:10.1016/0022-1694(91)90189-O.

686 Kjeldsen, P., P. L. Bjerg, K. Rügge, T. H. Christensen, J. K. and Pedersen, (1998), Characterization
687 of an old municipal landfill (Grindsted, Denmark) as a groundwater pollution source: Landfill
688 hydrology and leachate migration, Waste Management and Research, Vol 16, no. 1, pp. 14-22.,
689 doi:10.1177/0734242X9801600103.

690 Knupp, P. (1996), Moving mesh algorithm for 3-D regional groundwater flow with water table and
691 seepage face, Advances in Water Resources, Vol. 19, No. 2, Pages 83-95.

692 Krause, S., A. Bronstert and E. Zehe (2007), Groundwater-surface water interactions in a north
693 German lowland floodplain – Implications for the river discharge dynamics and riparian water
694 balance, Journal of Hydrology, Vol. 347, Pages 404-417, doi:10.106/j.jhdrol.2007.09.028.

695 Krause, S., T. Blume, and N. J. Cassidy (2012), Investigating patterns and controls of groundwater
696 up-welling in a lowland river by combining Fibre-optic Distributed Temperature Sensing with
697 observations of vertical hydraulic gradients, Hydorlogy and Hearth System Sciences, 16, 1775-
698 1792, doi:10.5194/hess-16-1775-2012.

699 Krause, S., F. Boano, M. O. Cutchbert, J. H. Fleckenstein and J. Lewandowski (2014), Understanding
700 process dynamics at aquifer-surface water interfaces: An introduction to the special edition
701 section on modeling approaches and novel experimental technologies, Water Resources
702 Research, Vol. 50, Pages 1847-1855, doi: 10.1002/2013WR014755.

703 Larkin R. G. and J. M. Sharp (1992), On the relationship between river-basin geomorphology, aquifer
704 hydraulics, and ground-water flow direction in alluvial aquifers, Geological Society of
705 American Bulletin, V. 104, P. 1608-1620.

706 Lønborg, M.J., Engesgaard,P., Bjerg,P.L. & Rosbjerg,D. (2006): A steady state redox zone approach
707 for modeling the transport and degradation of xenobiotic organic compounds from a landfill
708 site. Journal of Contaminant Hydrology, 87, 191-210.

709 Miracapillo, C., and H. J. Morel-Seytoux (2014), Analytical solutions for stream-aquifer flow
710 exchange under varying head asymmetry and river penetration: Comparison to numerical
711 solutions and use in regional groundwater models, Water Resour. Res., 50, 7430–7444,
712 doi:10.1002/2014WR015456.

713 Modica, E., H. T. Buxton and L. N. Plummer (1998), Evaluating the source and residence time of
714 groundwater seepage to streams, New Jersey Coastal Plan, Water Resources Research, Vol. 34,
715 No. 11, Pages 2797-2810.

716 Nalbantis, I., A. Efstratiadis, E. Rozos, M. Kopsiafti and D. Koutsoyiannis (2011), Holistic versus
717 monometric strategies for hydrological modelling of human-modified hydrosystems,
718 Hydrology and Earth System Sciences, Vol. 15, Pages 743-758, doi:10.5194/hess-15-743-2011.

719 Nash, J. E. and J. V. Sutcliffe (1970), River flow forecasting through conceptual models part I — A
720 discussion of principles, Journal of Hydrology, 10 (3), 282–290, doi: 10.1016/0022-
721 1694(70)90255-6

722 Ou, G., X. Chen, A. Kilic, S. Bartelt-Hunt, Y. Li and A. Samal (2013), Environmental Modelling &
723 Software, Vol. 50, Pages 132-143.

724 Poulsen, J. R., E. Sebok, C. Duque, D. Tezlaff and P. K. Engesgaard (2015), Detecting groundwater
725 discharge dynamics from point-to-catchment scale in a lowland stream: combining hydraulic
726 and tracer methods, Hydrology and Earth System Sciences, 19, 1871-1886, doi:10.5194/hess-
727 19-1871-2015

728 Rasmussen, J. J., U. S. McKnight, A. T. Sonne, P. Wiberg-Larsen and P. L. Bjer (2016), Legacy of a
729 chemical factory site: Contaminated groundwater impacts stream macroinvertebrates, Arch
730 Environ Contam Toxicol, doi: 10.1007/s00244-015-0211-2.

731 Revelli, R., F. Boano, C. Camporale, and L. Ridolfi (2008), Intre-meander hyporheic flow in alluvial
732 rivers, Water Resources Research, Vol. 44, doi:10.1029/2008WR007081.

733 Salehin, m., A. I. Packman, and M. Paradis (2004), Hyporheic exchange with heterogenous
734 streambeds: Laboratory experiments and modeling, Water Resources Research, Vl. 40,
735 W11504, doi:10.1029/2003WR002567.

736 Stonedahl, S. H., J. W. Harvey, A. Wörman, M. Salehin and A. I. Packman (2010), A multistate
737 model for integrating hyporheic exchange from rippleds to meanders, Water Resources
738 Management, Vol. 46, W12539, doi:10.1029/2009/WR008865.

739 Sugio S. and C. S. Desai (1987), Residual flow procedure for sea water intrusion in unconfined
740 aquifers, journal of numerical methods in engineering, Vol. 24, 1439-1450.

741 Toth, J. (1963), A Theoretical Analysis of Groundwater Flow in Small Drainage Basins, Journal of
742 Geophysical Research, Vol. 68, No. 16, Pages 4795-4812.

743 Walther, M., J.-O. Delfs, J. Grundmann, O. Kolditz, and R. Liedl (2012), Saltware intrusion
744 modeling: Verification and application to an agricultural coastal arid region in Oman, Journal
745 of Computational and Applied Mathematics, 236, 4798-1809, doi:10.1016/j.cam.2012.02.008.

746 Weatherill, J., S. Krause, K. Voyce, F. Drijfhout, A. Levy and N. Cassidy (2014), Nested monitoring
747 approaches to delineate groundwater trichloroethene discharge to a UK lowland stream at
748 multiple spatial scales, Journal of Contaminant Hydrology, Vol. 158, Pages 38-54.

749 Wroblicky, G. J., M. E. Campana, H. M. Valett and C. N. Dahm (1998), Seasonal variation in surface-
750 subsurface water exchange and lateral hyporheic area of two stream-aquifer systems, Water
751 Resources Research, Vol. 34, No. 3, Pages 317-328

752

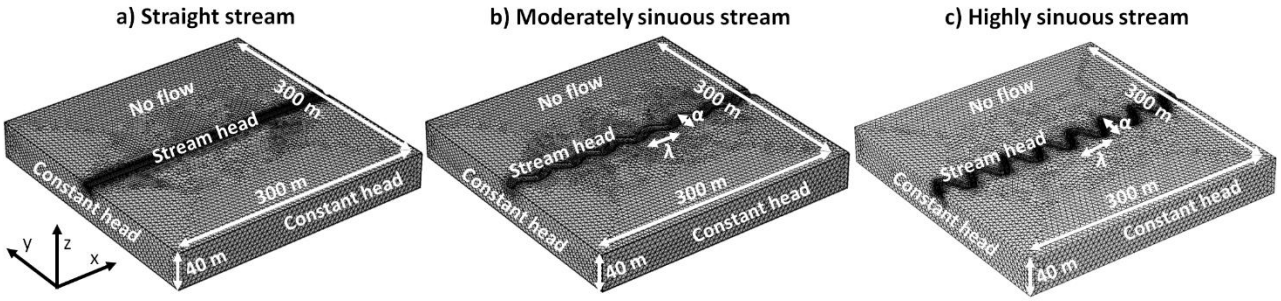

Figure 1: Model domain, finite element mesh, and boundary conditions for the three scenarios of the synthetic stream model: straight stream (a), the moderately sinuous stream (b), and the highly sinuous stream (c) models.

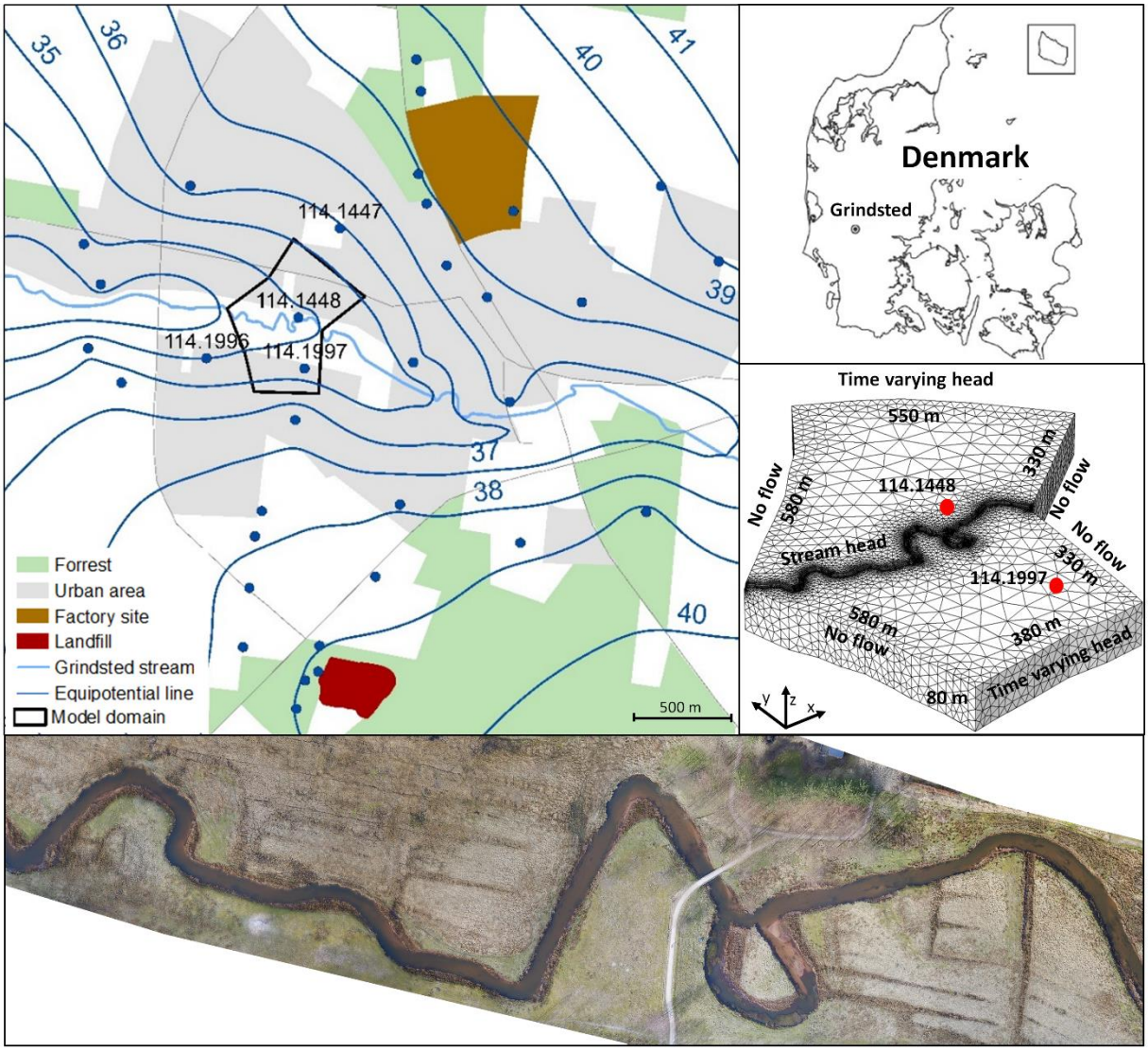

Figure 2: Overview of the Grindsted stream study site and model set up. The blue lines indicate the equipotential lines with an interval of 1 m. The equipotential map is based on groundwater head measurements collected at the wells indicated by the blue dots. The name of the observation wells used to set up boundary conditions or for comparison with model results are shown on the map. The model domain area is defined by the black line. The bottom figure shows an orthophoto of the simulated stream reach. The middle right figure shows the model grid, the boundary conditions, the model size, and the location of boreholes in the model domain.

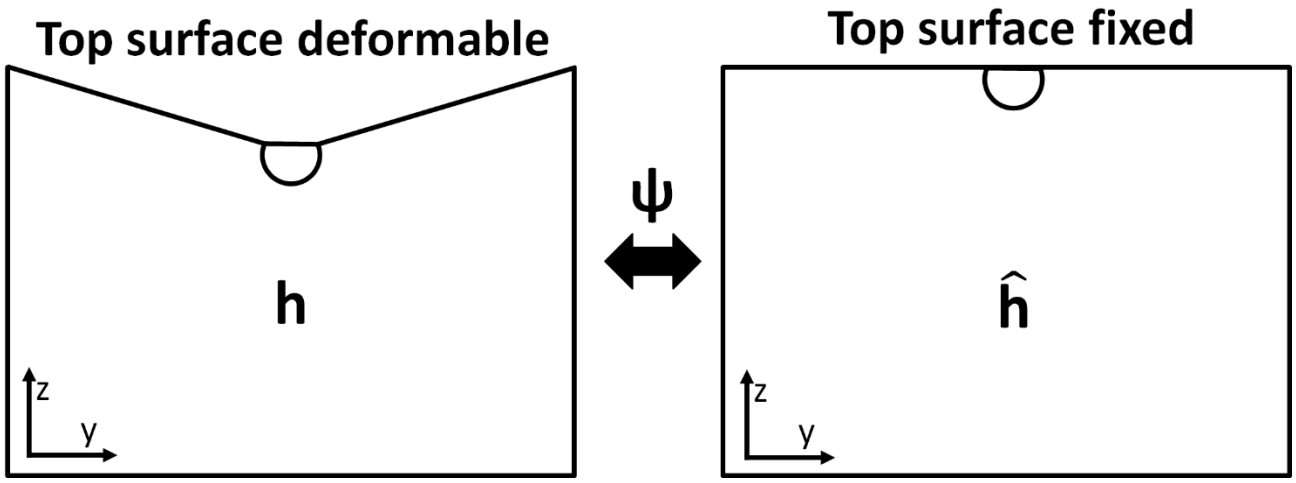

763

764 **Figure 3: The coordinate transformation method for modeling unconditioned aquifers interacting with streams of Boon et al.**
765 **(2016) employs a fixed domain (right) instead of the real deformable domain (left). A coordinate transformation Ψ is used to**
766 **map the governing equations between the two domains.**

767

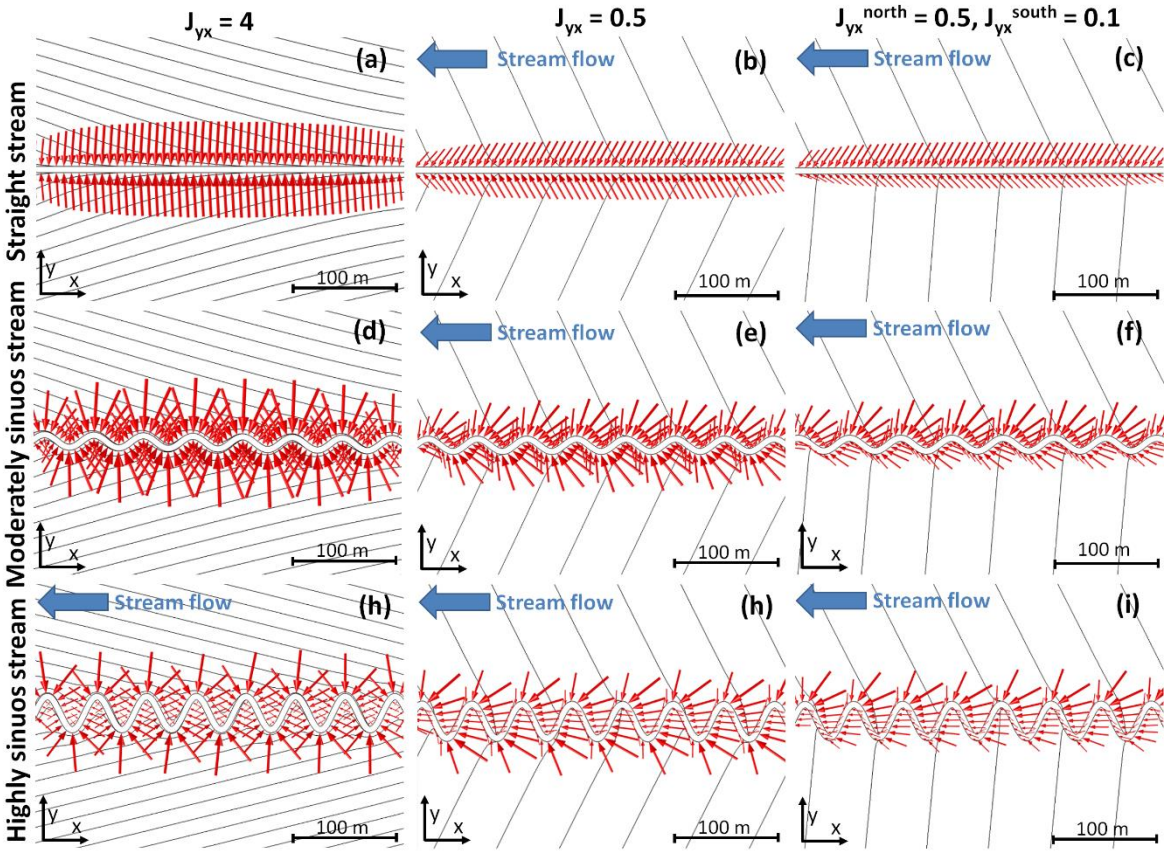

768

769 **Figure 4: Groundwater discharge to the stream at the upper edge of the stream-aquifer interface shown by the red arrows,**
770 **which are proportionate to the flow. The equipotential lines are indicated by the black lines and are separated by 0.05 m**
771 **interval. Jyx represent the ratio between the hydraulic gradient in the y and in x-direction. The moderately sinuous stream has**
772 **sinuosity (S) of 1.14 and amplitude (α) of 5 m. The highly sinuous stream has sinuosity (S) of 1.74 and amplitude (α) of 13.5 m.**

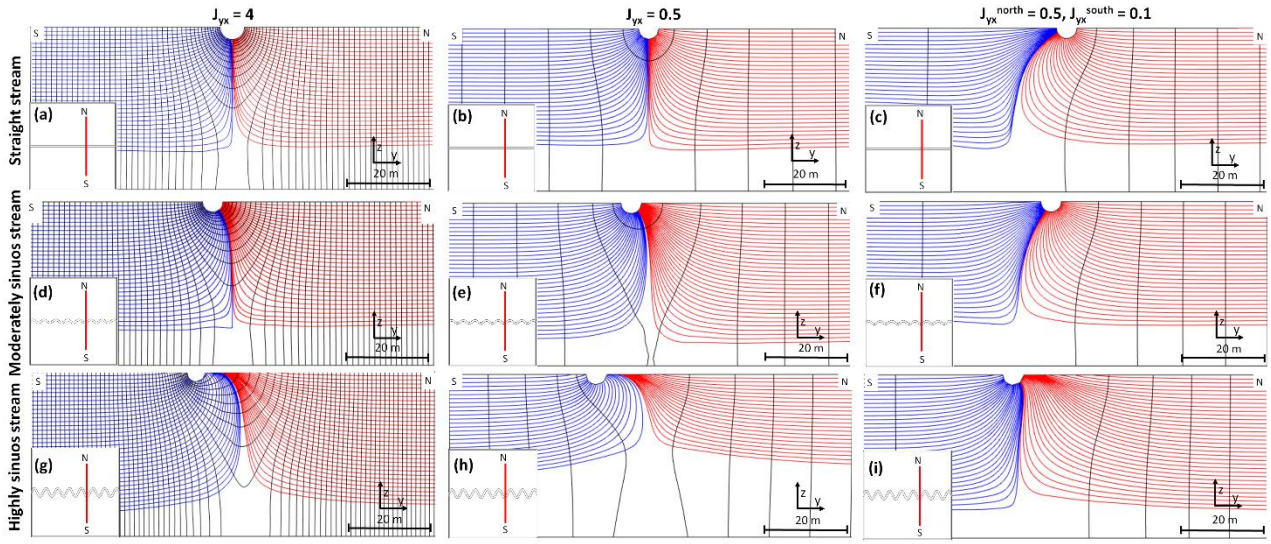

Figure 5: Groundwater paths from the northern (red lines) and southern (blue lines) sides of the stream at a vertical cross section perpendicular the stream located at the edge of a meander pointing south. The black lines show the equipotential lines separated by 0.005 m. Jyx represent the ratio between the hydraulic gradient in the y and in x-direction. The moderately sinuous stream has sinuosity (S) of 1.14 and amplitude (α) of 5 m. The highly sinuous stream has sinuosity (S) of 1.74 and amplitude (α) of 13.5 m

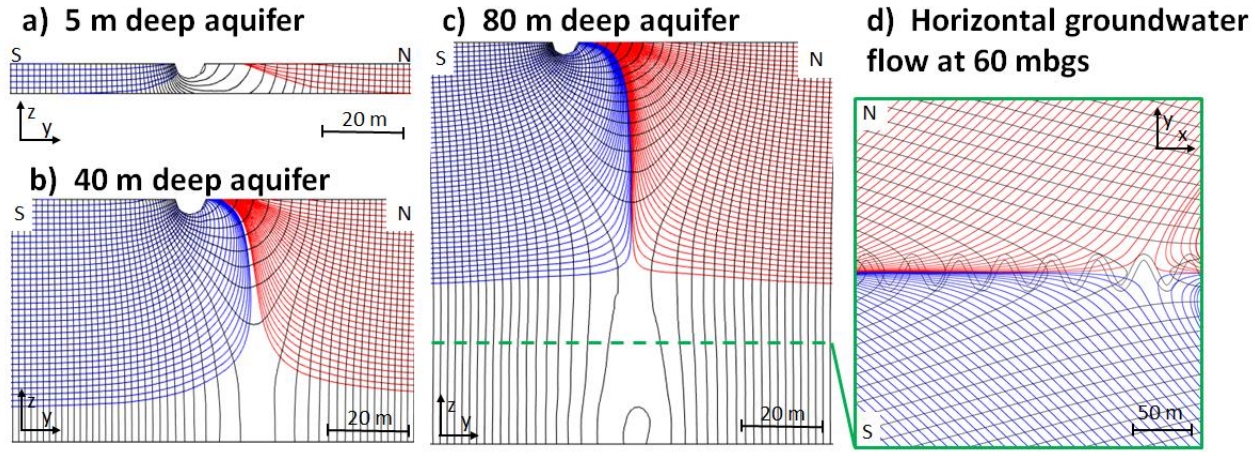

Figure 6: Effect of the aquifer thickness on the groundwater paths from the northern side of the stream (red lines) and from the southern side of the stream (blue lines) at three vertical cross sections perpendicular the stream and located at the edge of a meander bend pointing south (a, b, and c). The black lines show the equipotential lines separated by 0.005 m interval. The green line in the 80 m deep aquifer (c) show the depth of the plan view section (d). The highly sinuous stream scenario with a J_{yx} of 4 was employed.

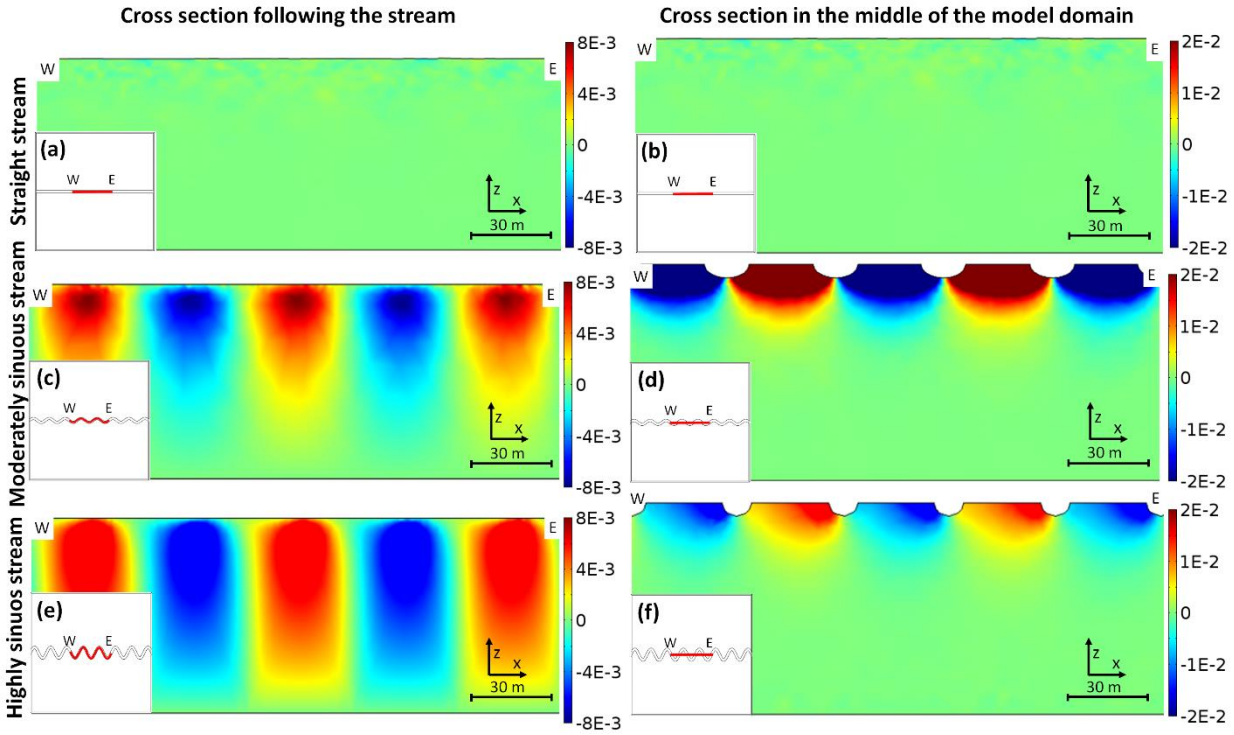

Figure 7: Groundwater flow in the y direction (q_y) in m/s through vertical cross sections along the stream: the left panels show cross sections that follow the meandering stream path (a, c, and e), while the right hand panels show straight cross sections centered in the middle of the model domain (b, d, and f). Positive flow is directed to the north. The results are shown for the straight, the moderately sinuous and the highly sinuous stream with J_{yx} = 0.5 and an aquifer thickness of 40 m. The moderately sinuous stream has sinuosity (S) of 1.14 and amplitude (α) of 5 m while the highly sinuous stream has a sinuosity (S) of 1.74 and amplitude (α) of 13.5 m.

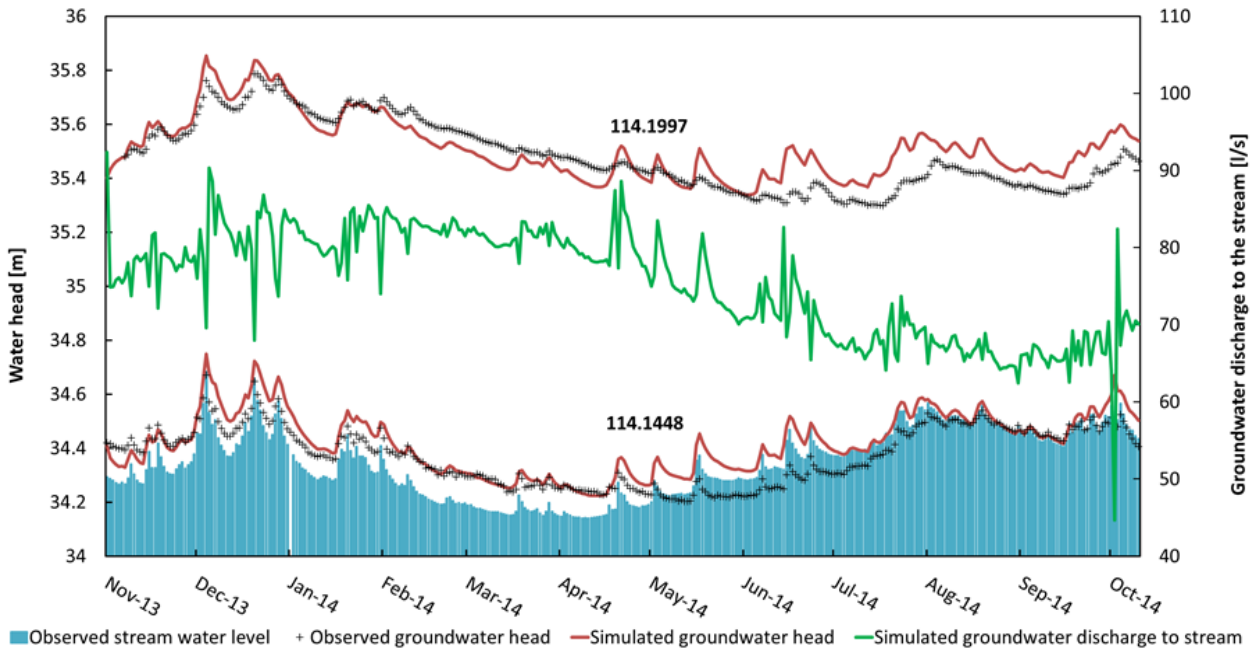

Figure 8: Model results from Grindsted stream compared to groundwater head data from well 114.1448 and 114.1997 (Figure 2). The stream water level at the closest location to well 114.1448 is indicated by the blue columns. The stream water level was calculated from the water level measurements at the Tingvejen station assuming a stream water slope, which was calculated at each day from the water level measurements at the Tingvejen and the Eg bro stations. The groundwater discharge to the stream (green line) is plotted to the secondary y-axes, which starts at 40 l/s, and is the integrated value of the discharges along the modeled stream stretch.

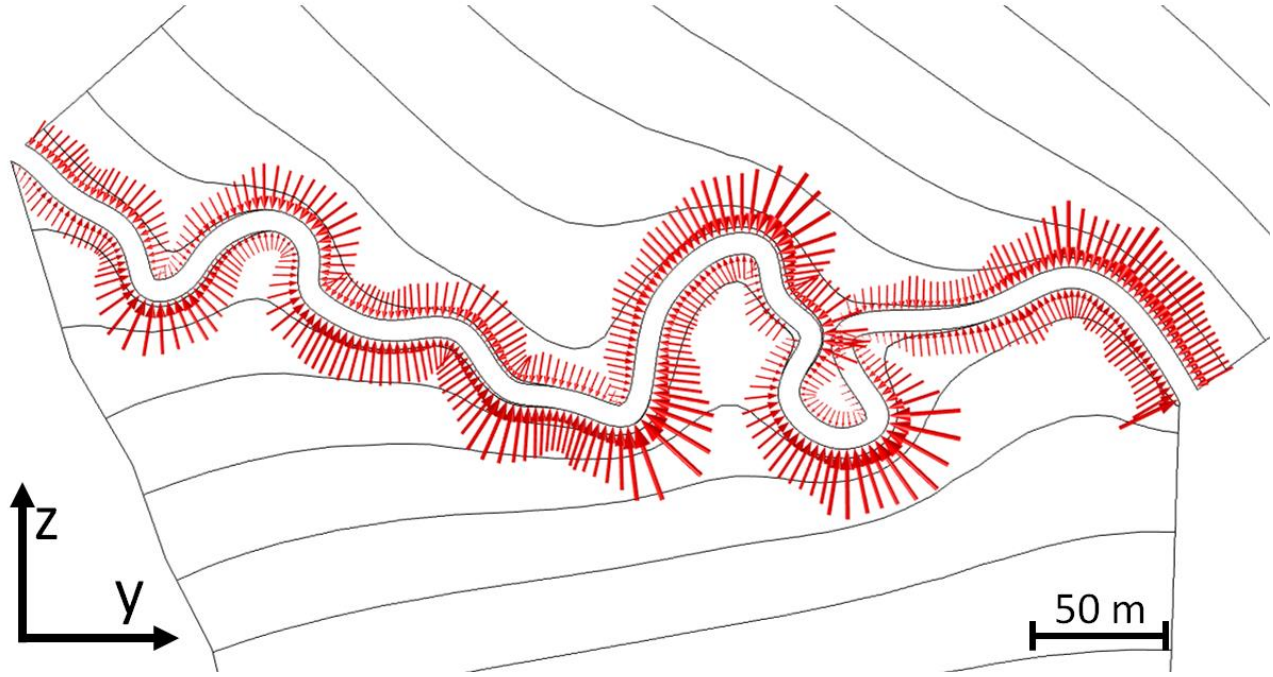

Figure 9: Horizontal groundwater flow at the upper edge of the stream-aquifer interface. The red arrows are proportional to the fluxes. The equipotential lines are separated by 0.2 m.

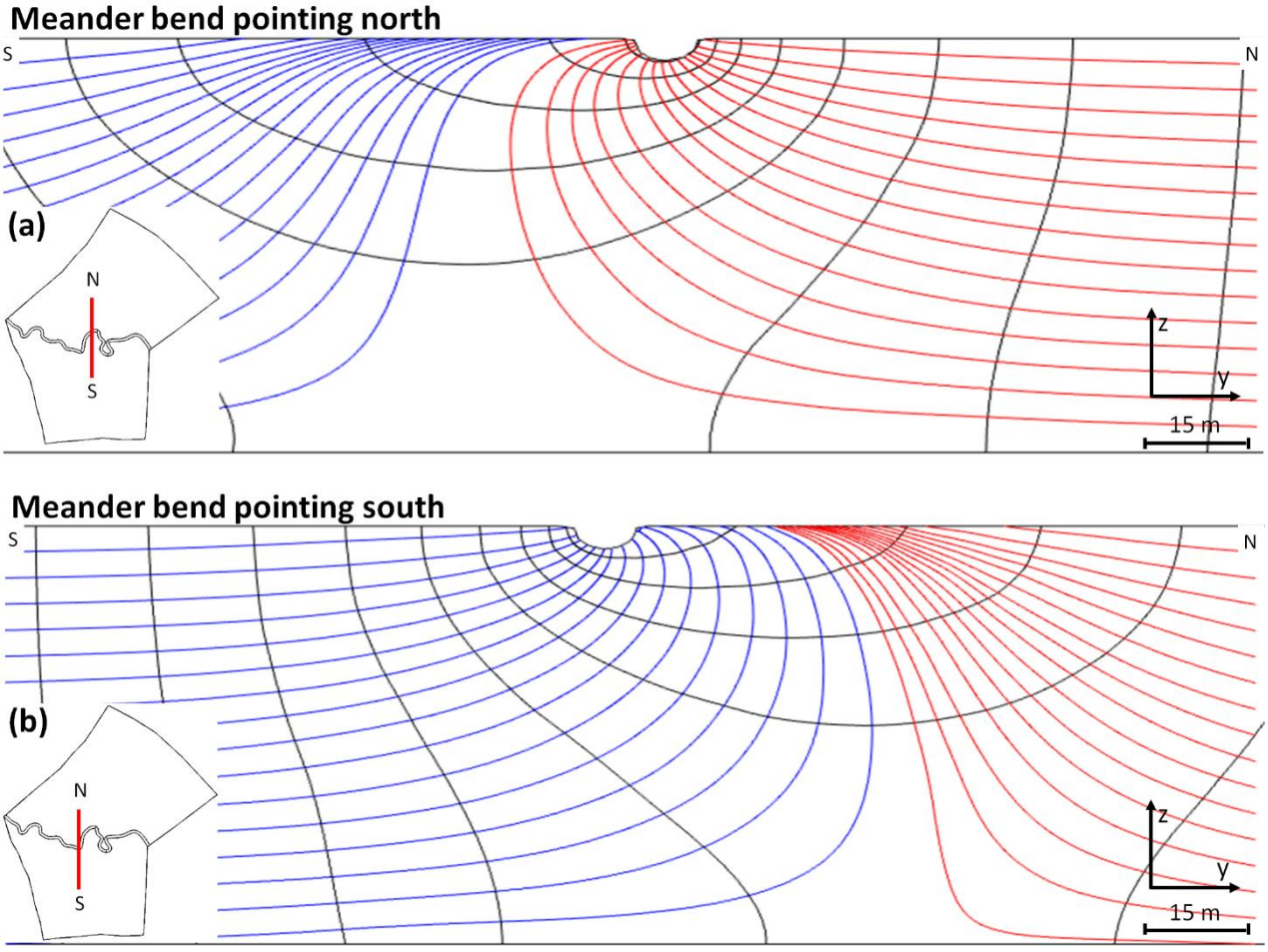

807

808 **Figure 10: Groundwater paths from the northern side of the stream (red lines) and from the southern side of the stream (blue**
809 **lines) at two vertical cross sections perpendicular the stream and located at the edge of a meander bend pointing north (a) and**
810 **south (b). The black lines show the equipotential lines with a 0.1 m interval.**

811